Cancer Cell

Article

# Chemotherapy induces myeloid-driven spatially confined T cell exhaustion in ovarian cancer

## Graphical abstract

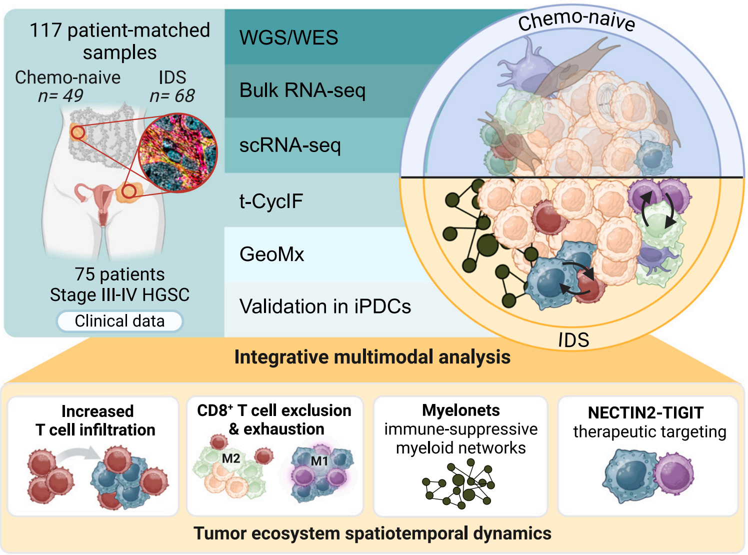

## Highlights

- Spatial analysis reveals myeloid-driven CD8$^+$ T cell exhaustion post-chemotherapy
- Myelonets are key compartments driving immune suppression in HGSC
- CD8$^+$ T cell exhaustion and exclusion link to poor chemotherapy response
- NECTIN2-TIGIT signaling predicts preclinical immune checkpoint blockade response

## Authors

Inga-Maria Launonen, Iga Niemiec,
María Hincapié-Otero, ...,
Peter K. Sorger, Anna Vähärautio,
Anniina Färkkilä

## Correspondence

anna.vaharautio@helsinki.fi (A.V.),
anniina.farkkila@helsinki.fi (A.F.)

## In brief

Spatial and molecular profiling of 117 tumors before and after chemotherapy reveals a dynamic tumor ecosystem in ovarian cancer. Launonen et al. identify Myelonets as drivers of CD8$^+$ T cell exhaustion and demonstrate that NECTIN2-TIGIT signaling predicts preclinical immune checkpoint blockade response, unlocking new therapeutic strategies for high-grade serous carcinoma.

Launonen et al., 2024, Cancer Cell *42*, 2045–2063

https://doi.org/10.1016/j.ccell.2024.11.005

Cancer Cell

CellPress
OPEN ACCESS

Article

# Chemotherapy induces myeloid-driven spatially confined T cell exhaustion in ovarian cancer

Inga-Maria Launonen,[1] Iga Niemiec,[1,10] María Hincapié-Otero,[1,10] Erdogan Pekcan Erkan,[1,11] Ada Junquera,[1] Daria Afenteva,[1] Matias M. Falco,[1] Zhihan Liang,[1] Matilda Salko,[1] Foteini Chamchougia,[1] Angela Szabo,[1] Fernando Perez-Villatoro,[1] Yilin Li,[1] Giulia Micoli,[1] Ashwini Nagaraj,[1] Ulla-Maija Haltia,[1,2] Essi Kahelin,[1,3] Jaana Oikkonen,[1] Johanna Hynninen,[4] Anni Virtanen,[1,3] Ajit J. Nirmal,[5] Tuulia Vallius,[5,6] Sampsa Hautaniemi,[1] Peter K. Sorger,[5,6] Anna Vähärautio,[1,7,*] and Anniina Färkkilä[1,2,8,9,12,*]

[1]Research Program in Systems Oncology, University of Helsinki, Helsinki, Finland
[2]Department of Obstetrics and Gynecology, Department of Oncology, Clinical Trials Unit, Comprehensive Cancer Center, Helsinki University Hospital, Helsinki, Finland
[3]Department of Pathology, University of Helsinki and HUS Diagnostic Center, Helsinki University Hospital, Helsinki, Finland
[4]Department of Obstetrics and Gynecology, University of Turku and Turku University Hospital, Turku, Finland
[5]Laboratory of Systems Pharmacology, Harvard Medical School, Boston, MA, USA
[6]Ludwig Center at Harvard, Boston, MA, USA
[7]Foundation for the Finnish Cancer Institute, Helsinki, Finland
[8]iCAN Digital Precision Cancer Medicine Flagship, Helsinki, Finland
[9]Institute for Molecular Medicine Finland, Helsinki Institute for Life Sciences, University of Helsinki, Helsinki, Finland
[10]These authors contributed equally
[11]Present address: Faculty of Medicine and Health Technology, Tampere University, Tampere, Finland
[12]Lead contact
*Correspondence: anna.vaharautio@helsinki.fi (A.V.), anniina.farkkila@helsinki.fi (A.F.)
https://doi.org/10.1016/j.ccell.2024.11.005

## SUMMARY

Anti-tumor immunity is crucial for high-grade serous ovarian cancer (HGSC) prognosis, yet its adaptation upon standard chemotherapy remains poorly understood. Here, we conduct spatial and molecular characterization of 117 HGSC samples collected before and after chemotherapy. Our single-cell and spatial analyses reveal increasingly versatile immune cell states forming spatiotemporally dynamic microcommunities. We describe Myelonets, networks of interconnected myeloid cells that contribute to CD8$^+$ T cell exhaustion post-chemotherapy and show that M1/M2 polarization at the tumor-stroma interface is associated with CD8$^+$ T cell exhaustion and exclusion, correlating with poor chemoresponse. Single-cell and spatial transcriptomics reveal prominent myeloid-T cell interactions via NECTIN2-TIGIT induced by chemotherapy. Targeting these interactions using a functional patient-derived immuno-oncology platform demonstrates that high NECTIN2-TIGIT signaling in matched tumors predicts responses to immune checkpoint blockade. Our discovery of clinically relevant myeloid-driven spatial T cell exhaustion unlocks immunotherapeutic strategies to unleash CD8$^+$ T cell-mediated anti-tumor immunity in HGSC.

## INTRODUCTION

Tumorigenesis and cancer progression rely on malignant cells evading the host's immune system through complex spatial interactions among cell populations. T cell exhaustion, caused by chronic antigen stimulation, leads to hypofunctional T cells, some of which can be reinvigorated by immune checkpoint blockade (ICB) therapies.[1] While ICB therapies are widely used in oncology,[2,3] they have not been successful in unselected ovarian cancer patients.[4–7]

High-grade serous ovarian cancer (HGSC), the most common ovarian cancer subtype, is a highly aggressive disease characterized by ubiquitous deleterious mutations in *TP53*,[8] genomic instability,[9] and high tumor heterogeneity,[10] with the lack of recurrent genomic alterations.[11] First-line neoadjuvant chemotherapy (NACT) is commonly administered to patients with unresectable disease or comorbidities.[12,13] Regardless of the responses to first-line platinum-based chemotherapy, treatment resistance eventually develops in the majority of the patients.[14]

Anti-tumor immunity plays a critical role in HGSC therapy responses and clinical outcomes,[15–20] yet little is known how it is modulated by standard chemotherapy. We recently have shown that NACT enriches a stressed state in cancer cells, associated with immunocompromised macrophages and CD8$^+$ T cells.[21] On the other hand, NACT has been found to potentiate the immune fitness of HGSC by inducing oligoclonal expansion of CD8$^+$ T cells, increased infiltration of natural killer (NK) cells,[22] CD4$^+$ T cell activation,[23] and skewing tumor-associated macrophages

(TAMs) toward a proinflammatory phenotype, which may potentiate adaptive immune responses.[24]

Developments in spatial technologies enable detailed exploration of cellular phenotypes within tumor microenvironment (TME) niches.[25,26] It has been demonstrated that spatial localization dictates cellular phenotypes[27,28] and that spatial interactions play a crucial role in how tumor cells evade immune attack.[29,30] Importantly, the efficacy of ICBs depends on the spatial interactions between neighboring cells with distinct activation states,[31,32] which are reflected in the multicellular organization of the tumors.[33] We previously identified a TME phenotype with increased spatial immunosurveillance and prognostic implications in *BRCA*1/2-deficient HGSCs.[15] Additionally, we showed that responses to ICB and PARP inhibitors are shaped by the functional and spatial immune microenvironment.[16] Limited translational data from the Javelin Ovarian 200 and IMagyn050 trials suggest that patients with high CD8$^+$ T cell infiltration or elevated PD-L1 expression benefit from ICB when combined with chemotherapy.[5,6] To enhance ovarian cancer therapies, a deeper understanding of spatial dynamics in tumor ecosystem remodeling during chemotherapy is essential.

Here, we incorporate multi-omics profiling using genomics, single-cell RNA sequencing (scRNA-seq), high-dimensional whole-section tissue imaging, and spatial transcriptomics from 117 patient samples capturing over 25 million single cells and 316 spatial transcriptomic domains captured by molecular profiling. By combining genomic, single-cell, and spatial data from patient-matched HGSC samples collected before and after platinum-based chemotherapy, we show how the spatially resolved cell-cell interaction neighborhoods and transcriptional programs change dynamically during NACT, resulting in targetable, myeloid-driven spatially confined T cell exhaustion patterns. Our findings reveal new opportunities for patient stratification and targets for anti-tumor immunotherapies in ovarian cancer.

## RESULTS

### Multi-omic characterization reveals augmented immune infiltration during NACT

We collected a series of 117 spatiotemporally distinct tumor samples from 75 HGSC patients from two prospective observational clinical trials (NCT04846933 and NCT0611738) (Figures 1A and 1B). Detailed clinical characteristics, including anti-cancer treatments (chemotherapy, PARPi, bevacizumab), as well as surgical and survival outcomes were collected (summarized in Tables 1 and S1). The tumor samples were subjected to multi-omics profiling with whole-genome/exome sequencing (WGS/WES), RNA-seq, scRNA-seq, high-plex cyclic immunofluorescence (t-CyCIF) imaging, and spatial transcriptomics (Figure 1B).

Employing whole-slide t-CyCIF imaging to profile the spatial architecture of the single-cell TME, we first successfully identified and analyzed 6,402,172 cells across 22 tumor samples. We phenotyped 2,684,155 tumor cells, 2,060,194 stromal cells, and 1,657,823 immune cells by using our dedicated open-source package TRIBUS[34] (STAR Methods) and further annotated them into distinct functional metaclusters (Figures 1C and S1A–S1C, STAR Methods).

Using scRNA-seq, we analyzed 51 HGSC tumor samples (Figure S1D) from 29 HGSC patients, including both treatment-naive and NACT-treated (Figure S1E) tumors or ascites, yielding 136,452 cells, which included 25,091 epithelial/tumor cells, 13,952 stromal cells, and 97,409 immune cells using cluster annotations for canonical markers.[21] We used the CellTypist algorithm[35] to robustly identify immune cell subpopulations (Figure S1F, STAR Methods) and then aggregated them to match the higher hierarchy in the t-CyCIF data, facilitating scRNA-seq integration (Figures 1D and 1E). Further, we inferred cell populations from bulk RNA-seq data via Kassandra deconvolution (STAR Methods). The cell type proportions from patient- and site-matched samples showed significant correlations across t-CyCIF, scRNA-seq, and bulk RNA-seq data, particularly among the most common cell types (Figures S1G and 1F).

To assess the cell population dynamics during NACT, we integrated the populations from our multi-modal omics data. As an expected effect of chemotherapy, the tumor cell fraction decreased significantly after NACT in all data modalities (Figure 1G). Aligning with previous results,[21,36] the abundance of the proliferating epithelial phenotype decreased after NACT, with a significant infiltration of CD8$^+$ T cells (Figures 1G and S1H–S1J). Additionally, chemotherapy induced an increased signal for B cells, regulatory T cells, and myeloid cells in bulk RNA-seq (Figure 1G) and an increase in mast cells, innate lymphoid cells (ILCs), and NK cells in scRNA-seq data (Figures S1J and S1K). We further compared cell type compositions between paired chemo-naive and respective interval debulking surgery (IDS) specimens to reveal potential patient-specific, stable features in TME composition from the scRNA-seq data. Fibroblast proportion significantly correlated between treatment-naive and respective IDS tumors, unlike the proportion of cancer cells, macrophages or CD8$^+$ T cells (Figure S1L). This suggests that the overall immune TME composition is not stable through chemotherapy. Collectively, these observations indicate a generally augmented infiltration and activation of the immune TME driven by chemotherapy rather than patient-specific initial TME composition.

### Chemotherapy drives spatial landscape changes in the TME

To systematically analyze the spatial landscapes of cell communities within the HGSC TME, we annotated 18 distinct spatial microcommunities or recurrent cellular neighborhoods (RCNs) by clustering the cell-type neighborhood matrix (STAR Methods). The resultant RCNs included six tumor cell-dominated neighborhoods (RCN1-6), six stromal neighborhoods (RCN8-13), five immune neighborhoods (RCN14-18), and the tumor-stroma interface (RCN7) consisting of tumor, stromal, and immune cell subtypes (Figures 2A and 2B). Most of the immune-rich RCNs primarily consisted of myeloid cells; however, RCN17 was specifically enriched in T cells forming hubs within CD8$^+$ and CD4$^+$ T cells. After RCN17, the highest T cell infiltration occurred in the myeloid-rich neighborhoods RCN16, RCN18, and RCN14. (Figure S2A). To quantify RCN diversity, we used Rao's quadratic entropy of both cell type abundance and functional states.[37] RCN7, the tumor-stroma interface (TSI), exhibited the highest diversity in terms of cell types and marker expressions, while the RCN3 consisting of epithelial tumor cells had the lowest (Figure 2A), indicating that the RCN7 (TSI) portrays the highest potential for interactions across cell types. Importantly, clustering

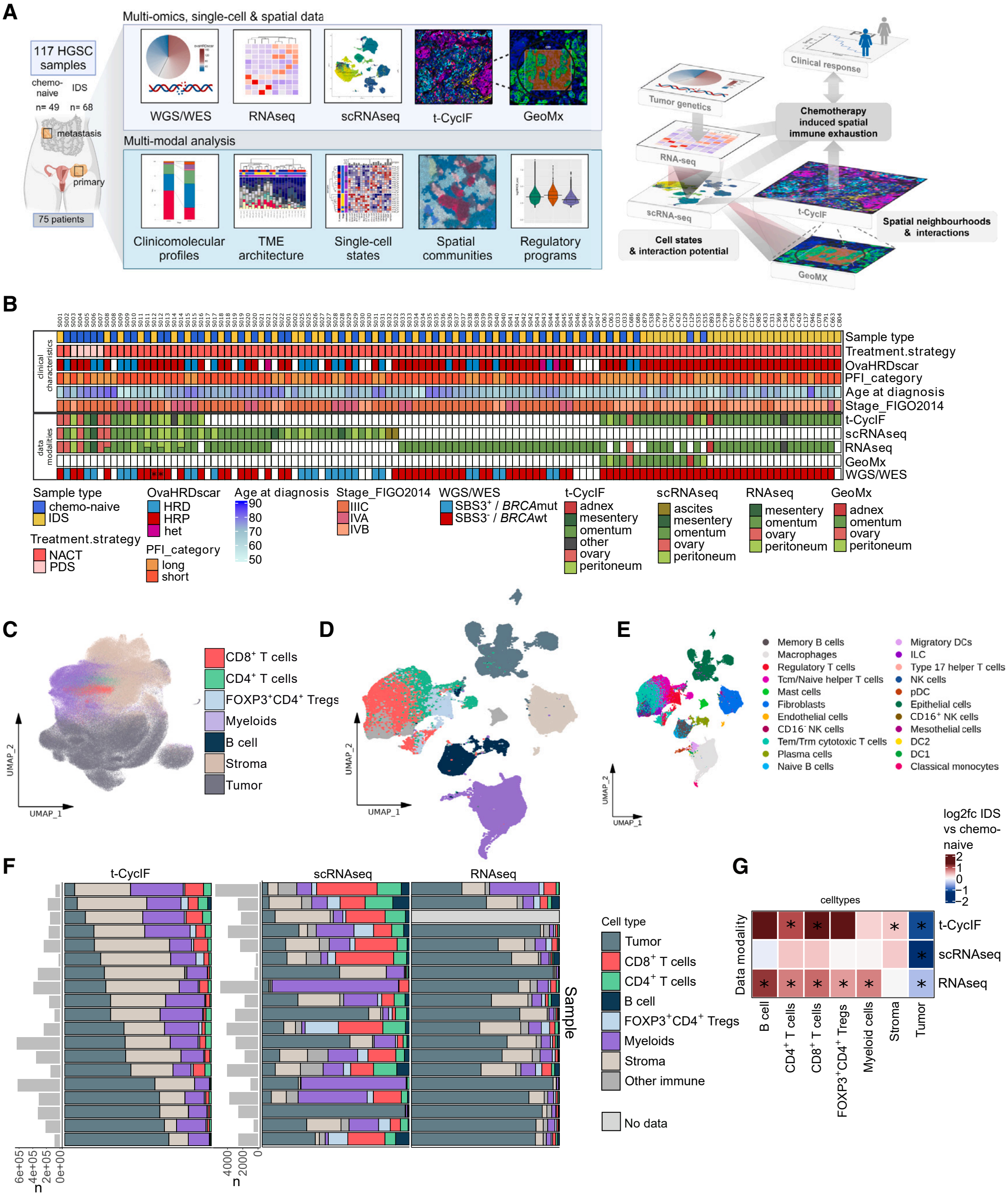

**Figure 1. Multi-omics characterization of the high-grade serous ovarian cancer (HGSC) tumor microenvironment (TME)**

(A) Schematic overview of the data and integration workflow.

(B) Dataset description and clinical features ($n = 117$ samples). The samples which were SBS3 negative but *BRCA* mutated are marked with an asterisk. HRD status was defined using ovaHRDscar.

(C and D) UMAP projection for cell types (C) in high-plex cyclic immunofluorescence (t-CycIF) data ($n = 22$ samples) and (D) in scRNA-seq data ($n = 51$ samples). The cell type annotation colors for (D) are the same as for (C).

(E) UMAP of fine-grained cell types in scRNA-seq data ($n = 51$ samples).

(F) Stacked bar plots of cell type proportions per sample for samples with patient- and site-matched t-CycIF, scRNA-seq, and RNA-seq data ($n = 19$ samples). On the x axis, n denotes the number of cells in t-CycIF and scRNA-seq data.

(G) Heatmap showing the log2 fold-change (fc) in interval debulking surgery (IDS) vs. chemo-naive cell type proportions (t-CycIF $n = 12$, scRNA-seq $n = 44$, RNAseq $n = 50$). Asterisk indicates $p$ value $< 0.05$ in paired Wilcoxon test.

See also Figure S1 and Table S1.

**Table 1. Patient clinical characteristics**

| Characteristic | N = 75[a] |
|---|---|
| Treatment strategy | |
| NACT | 70 (93%) |
| PDS[b] | 5 (6.7%) |
| NACT cycles | |
| 3 | 37 (53%) |
| 4 | 33 (47%) |
| NA | 5 |
| Surgery outcome | |
| R = 0 | 24 (35%) |
| R < 1 | 29 (43%) |
| R $\geq$ 1 | 15 (22%) |
| Unknown | 7 |
| CRS | |
| 1 | 11 (22%) |
| 2 | 34 (69%) |
| 3 | 4 (8.2%) |
| Unknown | 26 |
| PARPi | |
| no | 67 (89%) |
| yes[c] | 5 (6.7%) |
| unknown[d] | 3 (4.0%) |
| PARPi line | |
| 1 | 3 (60%) |
| 2 | 1 (20%) |
| after relapse | 1 (20%) |
| NA | 70 |
| RECIST response NACT | |
| CR | 6 (9.1%) |
| PR | 44 (67%) |
| SD | 14 (21%) |
| PD | 2 (3.0%) |
| Unknown | 9 |
| PFI (days) | 203 (83, 393) |
| BRCA result | |
| BRCAmut | 3 (4.3%) |
| gBRCAmut | 2 (2.9%) |
| BRCAwt | 65 (93%) |
| Unknown | 5 |
| HRD status | |
| HRD | 16 (23%) |
| HRP | 52 (73%) |
| Unknown | 7 (4%) |
| Age at diagnosis (years) | 69 (63, 74) |
| Stage | |
| IIIC | 36 (48%) |
| IVA | 11 (15%) |
| IVB | 28 (37%) |
| Bevacizumab maintenance | |
| yes | 43 (57%) |
| no | 32 (43%) |

See also Table S1.

[a] n (%); Median (Q1, Q3).

[b] were not used in paired analyses.

[c] at the time of sample collection, PARP-inhibitors were only reimbursed for patients with BRCAmut tumors.

[d] randomized clinical trial.

of the RCNs based on their spatial TME neighborhood compositions was driven by chemotherapy exposure (Figure 2C). The IDS samples contained a significantly decreased proportion of proliferating epithelial and epithelial cell enriched neighborhoods (RCN1 and RCN2) and increased proportions of myofibroblast (RCN12) and T cell enriched (RCN17) neighborhoods (Figure 2D).

We next assessed the effect of chemotherapy by hierarchical clustering of the cell-type proportions per RCN across the samples. Chemotherapy exposure significantly impacted (Fisher's exact test $p$ value $< 0.05$) the cell type compositions of three RCNs: RCN7 corresponding to the TSI, RCN14 characterized by M1-like ($IBA1^+CD11c^+$) macrophages, and the stromal neighborhood RCN8 (Figures 2E, S2B, and S2C). The cell type and state diversity itself of the tumor, immune, or stromal cell RCNs was not found to be influenced by chemotherapy, nor the heterogeneity of tumor, immune, or stromal cells irrespective of their spatial neighborhood (Rao's entropy score, data not shown). We next focused on the detailed characterization of the most diverse neighborhood RCN7 (highest Rao's entropy score). Chemotherapy exposure significantly impacted the cell-cell interaction enrichment and depletion patterns in the RCN7 (Figures 2F, 2G, S2D, and S2E). Permutation test statistics revealed chemotherapy-induced enhanced cell-cell interaction patterns between $CD8^+$ T cells neighboring M1 and M2-like myeloids and $CD4^+$ T cells (Figure 2G) whereas the chemo-naive samples displayed significantly more spatial interactions between $CD8^+$ T cells and the tumor metaclusters (Figure 2G). These observations indicate that $CD8^+$ T cells undergo an immunomodulatory neighborhood switch from tumor to myeloid interactions at the TSI during NACT (Figure 2H). This phenomenon was also validated in an independent HGSC cohort ($n = 8$ samples, four patient-matched chemo-naive-IDS pairs) analyzed with t-CyCIF (Figure S2F).

To investigate whether these $CD8^+$ T cell-myeloid interactions are associated with chemotherapy responses of the patients, we performed t-CyCIF analysis on 20 additional IDS samples from the Oncosys-OVA trial. Using single-cell and spatial analysis, we annotated matching RCNs within the TME (Figure S2G). Interestingly, enhanced $CD8^+$ T cell interactions with M2-like macrophages at the TSI were significantly associated with a shorter chemotherapy response (platinum free interval, PFI) (Figure 2I). Patients with long PFI presented enhanced interactions between $CD8^+$ T cells and tumor cells (Figure 2J) whereas the samples showing high M2-like to $CD8^+$ T cell interactions had significantly lower tumor cell to $CD8^+$ T cell interactions (Figure S2H).

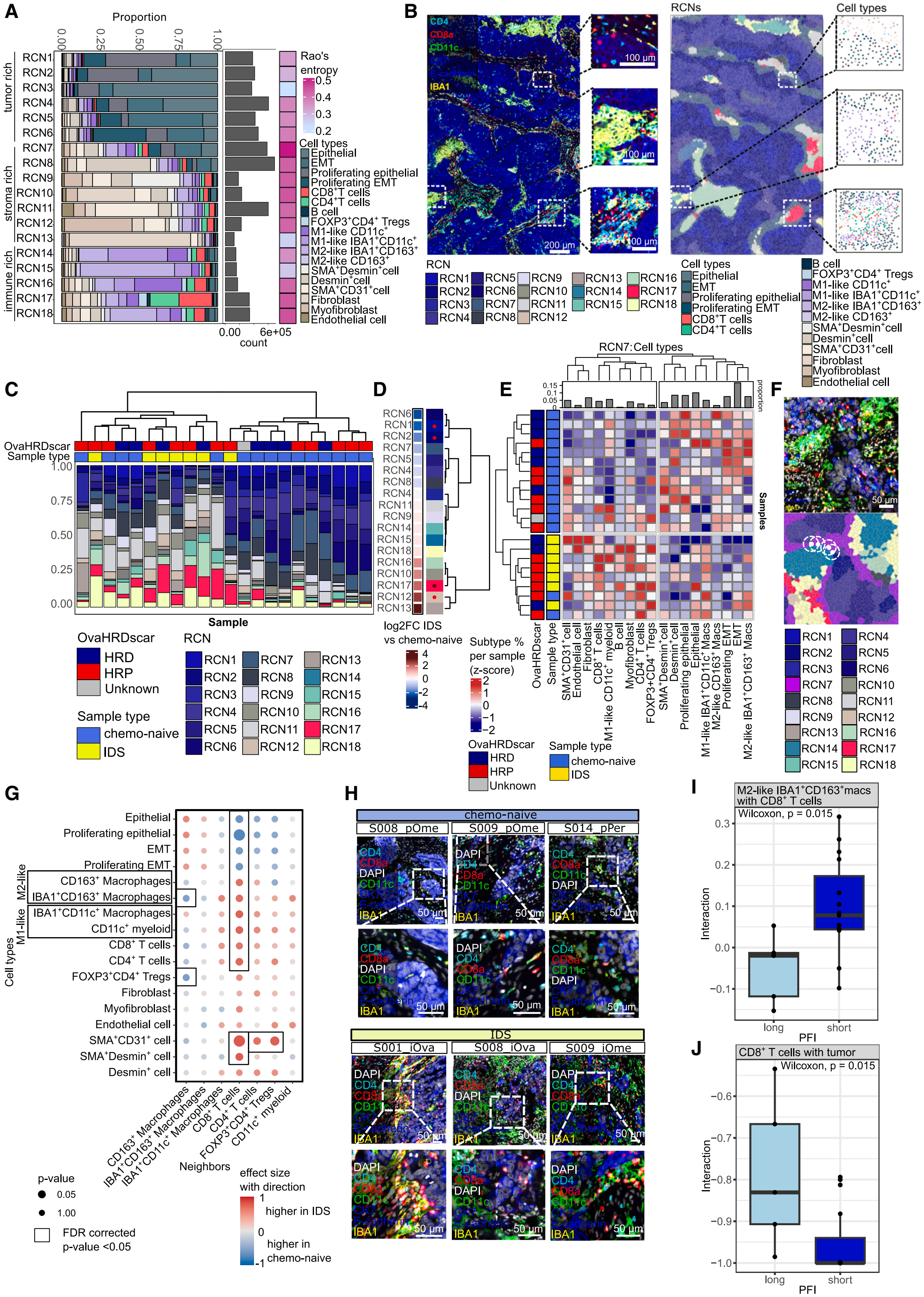

**Figure 2. Recurrent cellular neighborhoods (RCNs) uncover heterogeneous cellular architecture**

(A) Stacked barplot of the cell type composition of each RCN. The gray bar plot represents the total cell-type count in each RCN. The final annotation on the right represents Rao's entropy of each RCN.

(legend continued on next page)

In conclusion, the spatial neighborhood RCN7 (TSI) with the highest diversity and interaction potential, was the most responsive to change during chemotherapy. Chemotherapy led to increased interactions between $CD8^+$ T cells and myeloid cells at the TSI, wherein the M2-like interactions were associated with shorter responses to treatment. Conversely, sustained $CD8^+$ T cell - to tumor cell interactions were mutually exclusive with M2-like macrophage interactions and correlated with prolonged PFI. Altogether, these results implicate that M2-like macrophage interactions limit $CD8^+$ T cell interactions with tumor cells, resulting in inferior prognosis.

### Myeloid interactions shape the $CD8^+$ T cell phenotypes

Next, we investigated the spatial and functional dynamics of $CD8^+$ T cells and myeloid cells during chemotherapy. Remarkably, chemotherapy prompted a substantial spatial redistribution of the $CD8^+$ T cells within the RCNs (Figure 3A). In the chemo-naive samples, $CD8^+$ T cells predominantly occupied the T cell hubs (RCN17). In contrast, chemotherapy induced a significantly augmented infiltration of $CD8^+$ T cells across the myeloid RCNs and also many stromal and tumor RCNs (Figure 3A). Notably, along with the increased infiltration after NACT, the infiltrating $CD8^+$ T cells showed a distinctively exhausted ($TIM3^+$) phenotype and reduced activation state ($pSTAT1^+$) (Figures 3B, 3C, and S3A), suggesting that T cell exhaustion is spatially controlled. Altogether, our findings indicate that chemotherapy induces a transition from a spatially constrained immunophenotype to an immune-infiltrated TME.

As the T cell interactions showed evident spatial heterogeneity (Figure S3B), we next investigated how the spatial locations shaped their functional phenotypes during NACT. Interestingly, chemotherapy significantly induced the expression of the terminal exhaustion marker TIM3 in $CD8^+$ T cells residing in the two M1-like myeloid neighborhoods (RCN14 and RCN16), while the TIM3 expression decreased in the M2-type myeloid neighborhood (RCN15), as well as in T cell, tumor, and stromal-rich RCNs (Figure 3D). Chemotherapy also induced the expression of Ki67 and SNAT1 in $CD8^+$ T cells within all myeloid neighborhoods, with decreased pSTAT1, suggestive of TCR activation as a result of myeloid-T cell spatial crosstalk with compromised effector functionality.[38] The T cell memory marker CD45RO[39] increased only in RCN14 enriched in M1-like macrophages after NACT (Figure 3D). $CD8^+$ T cells in stromal neighborhoods harbored a quiescent state both before and after NACT. Our results indicate that NACT induces spatially restricted activation and exhaustion patterns in the TME, with exhausted $TIM3^+CD8^+$ T cells primarily in tumor islets before, and shifting toward myeloid neighborhoods after NACT.

We then assessed how interaction with distinct $CD8^+$ T cell states modified key macrophage phenotypes before and after chemotherapy (Figure S3C). Remarkably, MHC-II in macrophages exhibited the highest dependency on the $CD8^+$ T cell interaction especially after chemotherapy, indicating $CD8^+$ T cells priming by antigen-presenting macrophages. Chemotherapy enhanced the spatial interactions of activated macrophages (SNAT1, STAT1, and Ki67) with $CD8^+$ T cells (Figure S3C) whereas the phenotypes of cancer cells, interacting with distinct $CD8^+$ T cell states, remained unaffected (Figure S3D). Taken together, our results point toward functionally relevant spatial crosstalk between macrophages and $CD8^+$ T cells, resulting in enhanced activation and exhaustion of $CD8^+$ T cells during NACT.

### Myelonets—Interconnected functional networks of myeloid subpopulations

We observed that myeloid cells frequently form spatial clusters. Using Delaunay clustering, which identifies cells with direct cell-cell contacts, we uncovered spatial structures “Myelonets” that form interconnected myeloid networks consisting of more than nine interconnected myeloid cells (Figure 3E). The size of these networks ranged from small groups of ten to large Myelonets with thousands of cells independent of chemotherapy exposure. (Figures S3E–S3H) Myelonet size associated with their cellular composition, with the smallest Myelonets were identified inside RCN16 enriched in $CD11c^+$/M1myeloid cells (22 ± 20 cells) and RCN18 (78 ± 221 cells), containing also stromal and other immune cells. By contrast, the larger Myelonets were predominated by M1-like macrophages in RCN14 (mean 101 ± 412 cells), and M2-like macrophages in RCN15 (146 ± 379 cells) (Figure S3I). Hierarchical clustering of the myeloid cell functional states[40,41] across the Myelonets resulted in functional rather than patient-specific clusters, with M1-like Myelonets demonstrating the most active phenotype (Figure 3F). Functional marker expressions of the macrophages, $CD4^+$ and $CD8^+$ T cells inside Myelonets, was independent of the Myelonet size (data not shown).

We next looked into the distribution of the myeloid cells within and outside of the Myelonets. Indeed, large fractions (17–45%) of the myeloid cell subtypes resided inside the Myelonets (Figure 3G) which also contributed to a notable fraction of

---

(B) Representative image showing a high-plex cyclic immunofluorescence (t-CycIF) image on the left, and corresponding RCNs and individual cell types on the right.

(C) Barplot ordered by hierarchical clustering of the RCN proportions per sample (*n* = 22).

(D) Heatmap of the log2 fold-change in RCN proportions between chemo-naive (*n* = 6) and interval debulking surgery (IDS) samples (*n* = 6). Asterisk indicates *p* value <0.05 in paired Wilcoxon test.

(E) Heatmap showing row-wise *Z* scores for cell type proportions belonging to RCN7 per sample (*n* = 22) by hierarchical clustering.

(F) A representative t-CycIF image of a tumor area and neighboring stroma with the corresponding RCNs shown below. The neighboring cells for interaction analyses were performed with a 45 micron radius as depicted by the white dashed circles.

(G) Dot plot showing changes in cell-cell interactions in chemo-naive (*n* = 15) and IDS samples (*n* = 7) in the RCN7. *p* value from the Wilcoxon test.

(H) Representative images of the tumor stromal interface (TSI) and associated immune cell infiltrate in three chemo-naive and IDS samples.

(I and J) Boxplots showing spatial interaction with $CD8^+$ T cells and (I) $IBA1^+CD163^+$ macrophages and (J) tumor cells in short (*n* = 5) and long (*n* = 15) platinum free interval (PFI) groups. Black horizontal lines represent the sample medians, boxes extend from the first to the third quartile, and whiskers equals 1.5 interquartile range.

See also Figure S2.

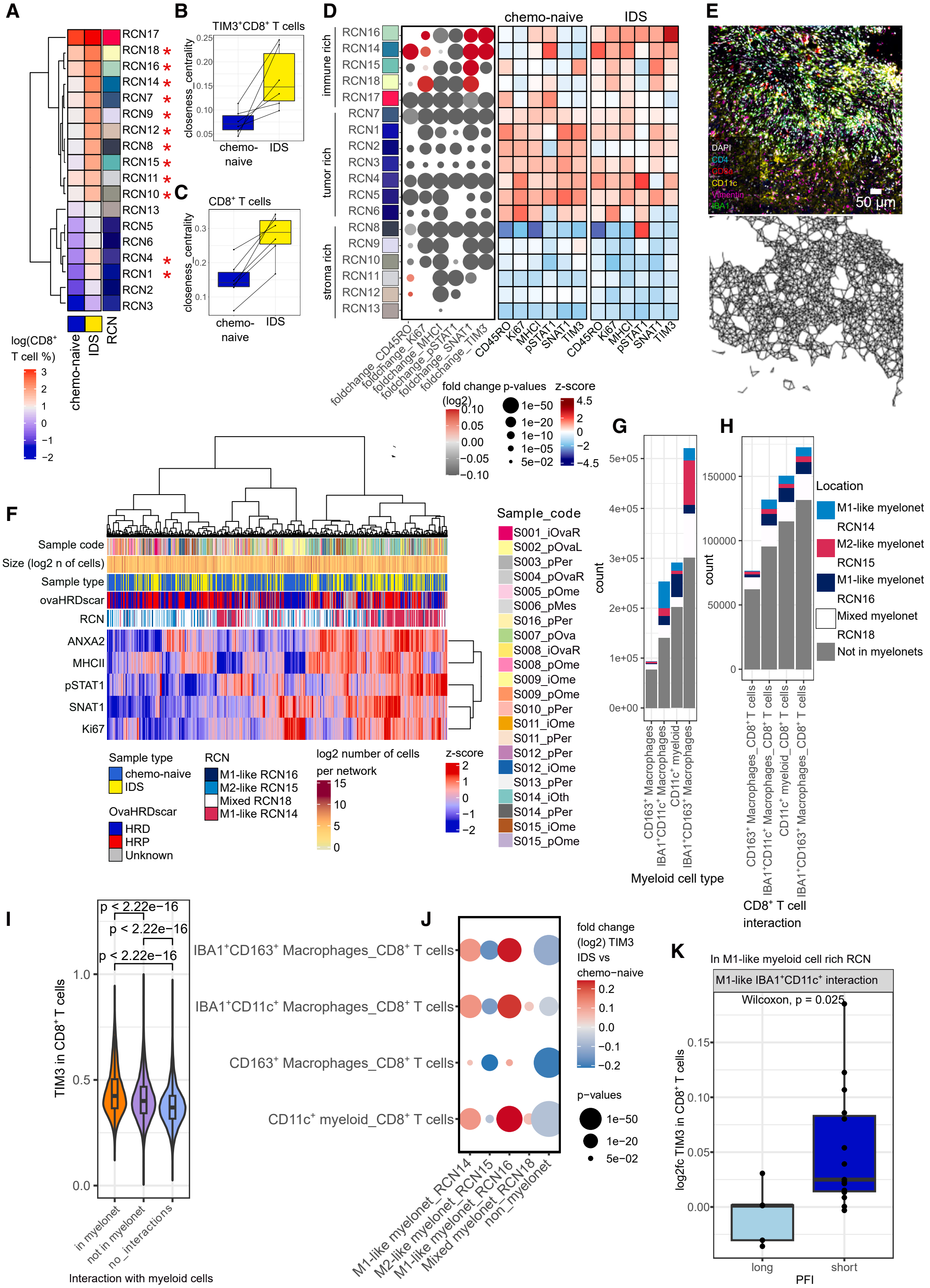

**Figure 3. Myeloid - CD8$^+$ T cell interplay within recurrent cellular neighborhoods (RCNs)**

(A) Heatmap of CD8$^+$ T cell proportions per RCN. Rows marked with an asterisk have a *p* value < 0.05 in the false discovery rate (FDR) corrected paired Wilcoxon test between chemo-naive (*n* = 6) and interval debulking surgery (IDS) samples (*n* = 6).

(legend continued on next page)

myeloid-T cell interactions (19–28%) (Figure 3H). Importantly, the Myelonets were significantly driving the exhaustion of the CD8$^+$ T cells: CD8$^+$ T cells interacting with myeloid cells within the Myelonets had a significantly higher TIM3 expression than CD8$^+$ T cells interacting with myeloid cells outside of the Myelonets or CD8$^+$ T cells not interacting with myeloid cells (Figure 3I). Chemotherapy-induced Myeloid-driven CD8$^+$ T cell exhaustion was particularly confined to the M1-enriched, RCN16 Myelonets (Figures 3J, S3J, and S3K). Moreover, this M1-like Myelonet-driven exhaustion was associated with a shorter PFI in our external dataset of 20 IDS tumors (Figure 3K). In summary, we find that Myelonets display as central hubs for T cell-myeloid interactions, driving T cell exhaustion, and contributing to poor chemotherapy responses within the chemotherapy-exposed TME of HGSC.

## Chemotherapy augments the interaction potential of macrophages and CD8$^+$ T cells

We next set out to explore the remodeling from the perspective of cell states on the scRNA-seq data layer using the Milo framework[42] to identify the potential reconditioning of cell states associated with chemotherapy in an unbiased manner (Figures 4A, S4A, and S4B). Interestingly, we evidenced an emergence of novel macrophage cell states after chemotherapy indicative of increased versatility. These states expressed increased levels of pro-inflammatory cytokines (Table S2) with tumor necrosis factor $\alpha$ (TNF-$\alpha$) and nuclear factor $\kappa$B (NF-$\kappa$B) pathway activity (Figure S4C), suggesting activation of inflammatory programs and the M1-like phenotype. Cytotoxic CD8$^+$ and naive CD4$^+$ helper T cells gained new states after chemotherapy with minimal loss of treatment-naive states, indicating NACT-induced versatility of also T cell states. In contrast, chemo-naive samples presented the majority of differentially abundant epithelial cell states, suggesting that in addition to lower abundance, the variety of cancer cell states diminishes after chemotherapy (Figures 4A, S4A, and S4B).

As chemotherapy shifted both cell state versatility (Figure 4A) and spatial CD8$^+$ T cell interactions (Figures 2 and 3) from cancer cells toward macrophages, we next analyzed how chemotherapy shapes intercellular crosstalk across these cells. By analyzing ligand-receptor interaction potential on paired scRNA-seq data from 22 patients with the MultiNicheNet framework[43] (STAR Methods), we discovered that in chemo-naive samples, cancer cell interactions involving cellular adhesion, integrins, and Notch signaling dominated the ligand-receptor crosstalk (Figure 4B). In the IDS samples, however, the dynamics were shifted toward macrophage-dominated signaling (Figure 4C), mirroring our observations on cell states (Figure 4A) and cellular interactions at the TSI (Figure 2G) The most strongly induced interaction from macrophages toward cytotoxic CD8$^+$ T cells was NECTIN2 binding to the competing activating receptor CD226[44,45] and repressive receptors CD96 and TIGIT (Figures 4D and S4D). Chemotherapy also induced MHC II-LAG3 interaction, associated with T cell exhaustion during prolonged antigen stimulation in cancer or chronic viral infection[46,47] and enhanced signaling toward the T cell adhesion and homing receptors CXCR4 and CD44.

To integrate the macrophage states with the t-CyCIF annotations, we confirmed that 96% of *AIF1* (encoding IBA1) expressing cells are macrophages, and assessed the M1-like and M2-like macrophage polarization axes in scRNA-seq data based on *ITGAX* (encoding CD11c) and *CD163* gene module scores, respectively (Figure 4E). Further analysis of the macrophage ligands revealed higher *NECTIN2* in the M1-like and *CXCL12* in the M2-like macrophages (Figure 4F). Notably, post-chemotherapy *CD163* gene module score (M2-like phenotype) was significantly higher in patients with short PFI (Figure 4G). This association was validated in the t-CyCIF data (Figure S4E) and specific to the IDS samples and the M2-like phenotype (Figure S4F).

To further investigate the CD8$^+$ T cell phenotypes and their interaction potential, we used the human CD8$^+$ T cell atlas[48] (Figure 4H). While *TIGIT* expression was enriched in precursor-exhausted (CD8.TPEX) CD8$^+$ T cells, *CD96* expression was specific to the terminally exhausted (CD8.TEX) population (Figure 4I). *CD226* expression was shared among the terminal effector memory T cells (CD8.TEMRA) and the exhausted populations. We further derived signatures for CD8$^+$ T cell populations positive for *TIGIT*, *CD96*, or *CD226*, as well as macrophages positive for *NECTIN2* (Table S2). In line with the CD8$^+$ T cell atlas projection, the *TIGIT*$^+$ CD8$^+$ T cells showed an increased expression of exhaustion markers *PDCD1* and *LAG3*, whereas the *CD226*$^+$ CD8$^+$ T cells expressed the tissue resident memory marker *ZNF683*. Moreover, *CD226*$^+$ CD8$^+$ cells overexpressed both cytotoxic molecules *GZMB* and *IFNG* as well as tumor infiltrating stem-like T cell population markers (*TCF7* and *PTGER2)*[49,50]

---

(B and C) Boxplots showing the closeness centrality as a measure of how close the group is to other nodes for (B) TIM3$^+$CD8$^+$ T cells and (C) CD8$^+$ T cells in IDS (*n* = 6) and chemo-naive (*n* = 6) samples. Black horizontal lines represent the sample medians, boxes extend from the first to the third quartile, and whiskers equals 1.5 interquartile range.

(D) Dot plot and heatmaps showing differences in CD8$^+$ T cell functional states across the RCNs. The dot plot shows the log2 fold-change in the mean marker expression in IDS to chemo-naive samples with FDR-corrected Wilcoxon *p* values as the size of the dot. Heatmaps show the columnwise *Z* scores of marker expressions in CD8$^+$ T cells in RCNs in chemo-naive and IDS samples, respectively.

(E) Representative t-CycIF image of Myelonets and cells belonging to RCN14 Myelonets connected using Delaunay triangulation.

(F) Heatmap with hierarchical clustering of the mean functional marker expression per individual Myelonet.

(G and H) Barplots showing (G) the location of different myeloid cell subtypes and (H) the location of myeloid- CD8$^+$ T cell interactions.

(I) Violin plot showing the expression of TIM3 in CD8$^+$ T cells interacting with myeloid cells inside or outside of myelonets, or without myeloid cell interactions with Wilcoxon test *p* values. Black horizontal lines represent the sample medians, boxes extend from the first to the third quartile, and whiskers equals 1.5 interquartile range.

(J) Dot plot showing the log2 fold-change and Wilcoxon test *p* values of TIM3 in CD8$^+$ T cells interacting with different myeloid cells inside the different Myelonets when comparing cells from IDS (*n* = 7) to chemo-naive (*n* = 15) samples.

(K) Boxplot showing the log2 fold change in TIM3 in CD8$^+$ T cells interacting vs. not-interacting with IBA1$^+$CD11c$^+$ macrophages in the RCN rich in CD11c$^+$ myeloid cells in patients with short (*n* = 5) and long (*n* = 15) platinum free interval (PFI). *p* value from the Wilcoxon test. Black horizontal lines represent the sample medians, boxes extend from the first to the third quartile, and whiskers equals 1.5 interquartile range.

See also Figure S3.

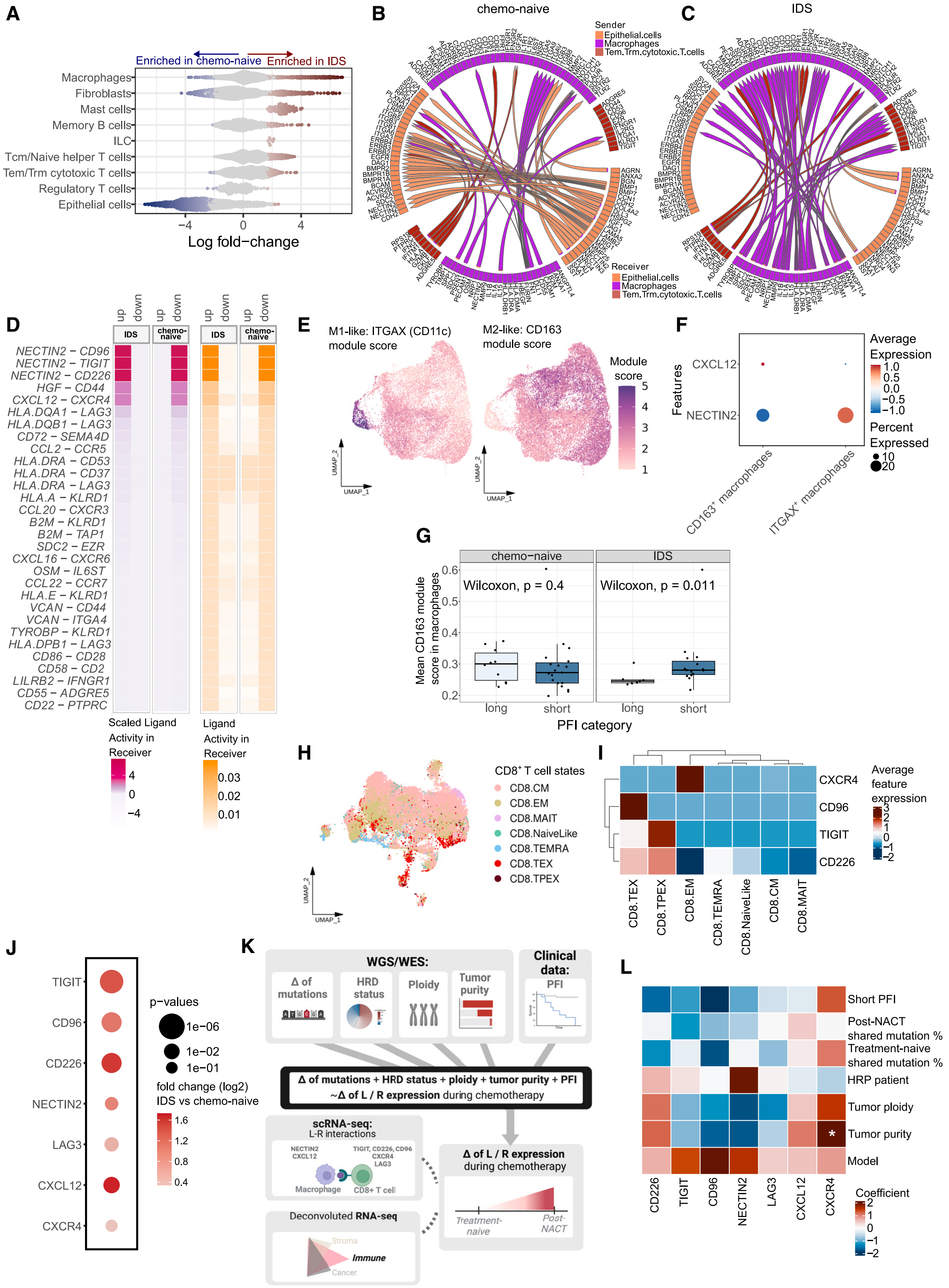

**Figure 4. Chemotherapy-associated dynamic changes in ligand-receptor interactions**

(A) Beeswarm plot showing the enrichment of cell state neighborhoods in chemo-naive (*n* = 22) and interval debulking surgery (IDS) (*n* = 22) samples. Light gray color denotes cell state neighborhoods with a false discovery rate (FDR) value > 0.05.

(B) Circos plot depicting the top 50 ligand-receptor interactions in (B) chemo-naive (*n* = 22) and (C) IDS samples (*n* = 22).

(legend continued on next page)

(Table S2). In summary, while the *CD226* co-activating receptor is expressed by CD8$^+$ T cells with markers of effective anti-tumor immunity, the checkpoint receptors *TIGIT* and *CD96* are expressed by increasingly exhausted CD8$^+$ T cell populations.

We also assessed these repressive and adhesive receptors in immune-deconvoluted[51] bulk RNA-seq in 50 paired, patient, and site-matched intra-abdominal metastases from the DECIDER trial. In line with the ligand-receptor analysis, chemotherapy significantly induced the immune expression of the repressive *TIGIT*, *CD96*, and *LAG3* and adhesive *CD226* receptors, as well as the expression of *NECTIN2* and the *CXCL12* chemokine (Figures 4J and S4G). Furthermore, chemotherapy increased the predicted activity of distinct transcription factors in immune-deconvoluted RNA-seq, promoting T cell exhaustion (*IRF4*),[52] inflammation, and immunity (*SPI1*, *FOXO3*, and *CEBPA*) (Figure S4H).

Considering that tumor genomics or patient clinical factors could influence the ligand-receptor dynamics, we next integrated the tumor genetic features (e.g., HR status or ploidy), NACT-induced genomic changes, and clinical characteristics of the patients (e.g., chemotherapy response) using linear mixed models (Figure 4K). For NACT-induced genomic changes, we used the proportion of mutations that each chemo-naive sample shares with its paired IDS sample, and vice versa, and added tumor purity as a variable to mitigate its potential confounding effect. After multiple testing correction, neither the model itself, as estimated by the F statistic, nor any of the variables independently were significant in explaining the observed changes of ligand or receptor expressions of interest (Figure 4L). Hence, tumor genomic features, mutational changes, or patient's response to chemotherapy fail to explain the identified NACT-induced immunomodulatory ligand-receptor dynamics.

## Transcriptional determinants of spatial myeloid-T cell crosstalk

To integrate the t-CyCIF and scRNA-seq findings, we performed t-CyCIF-guided spatial transcriptomics (GeoMx) in the Oncocys-OVA cohort using 16 whole-slide chemo-naive ($n$ = 5) and IDS ($n$ = 11) HGSC samples (Figure 1B; Table S1). To dissect the roles of spatial CD8$^+$ T cell-macrophage interactions at the TSI, we selected four types of regions of interest (ROIs) based on presence or absence of CD8$^+$ T cells and IBA1$^+$ macrophages (Figures 5A and S5A; Table S1) and applied our pipeline integrating t-CycIF images with GeoMx[53] (STAR Methods). Next, we collected the transcriptomic signals separately for tumor and stromal areas of interest (AOIs). In total, we captured the whole transcriptome signals from 316 AOIs with the average number of 7450 genes detected per AOI (Figure S5B).

To assess the activity of the key immune-related processes, we calculated the gene set variation analysis (GSVA) scores for 19 signatures connected with M1/M2 macrophage polarization, T cell exhaustion, antigen presentation, and interleukin 2 (IL2), TNF-$\alpha$, and interferon $\gamma$ (IFN-$\gamma$) signaling, separately for tumor and stromal ROIs. (Tables S3 and S4, STAR Methods). Reflecting our findings on T cell infiltration occurring outside the tumor neighborhoods (Figure 3A), we observed higher activities of most of the pathways in stromal rather than tumor ROIs (Figures S5C and 3C), and hence focused further on these stromal compartments. Here, we observed chemotherapy-induced enrichment of both pathways related to T cell exhaustion (CTLA-4, PD-1 signaling, and T cell apoptosis regulation) and M1 macrophage polarization, exclusively in the ROIs where CD8$^+$ T cells and IBA1$^+$ macrophages colocalized (Figure 5B). This suggests that chemotherapy induces a prominent M1 polarization colocalizing with exhausted CD8$^+$ T cells at the TSI (Figure 5B).

Next, to reveal processes influencing T cell exhaustion in the posCD8_posIBA1 areas, we computed the correlation coefficients of the GSVA scores between pathways (Figures S5D and S5E) and grouped them by shared underlying biological processes (Figures 5C and 5D, STAR Methods; Table S3). T cell exhaustion significantly correlated with M1 macrophage signature, MHC-I antigen presentation, IL2- JAK-STAT and IFN-$\gamma$ signaling in both treatment-naive and IDS samples, and epithelial to mesenchymal transition (EMT), TNF$\alpha$-NF$\kappa$B, and M2 macrophage signatures only prior, and MHC-II signaling only after chemotherapy (Figures 5C and 5D). This suggests that the chemotherapy-induced T cell exhaustion is likely driven by prolonged antigen presentation by M1-polarized myeloid cells, with potential links to immune stimulation via IL2-JAK-STAT and IFN-$\gamma$.[54]

We then leveraged the cell type-specific profiles from our scRNA-seq dataset to deconvolute the t- CyCIF-guided GeoMX data using BayesPrism.[55] Besides cell-type fractions (Figures S5F–S5H), we computed cell-type specific transcriptomic profiles (Figure 5E), allowing analysis of key pathway activities and scRNA-seq derived signatures separately in CD8$^+$ T cell

---

(D) The top 50 ligand-receptor interactions between macrophages and CD8$^+$ T cells in chemo-naive ($n$ = 22) and IDS ($n$ = 22) samples, their ligand activity, and scaled ligand activity scores.

(E) UMAP plots showing *CD163* and *ITGAX* gene module scores in macrophages. Color scale represents the magnitude of the score.

(F) Dot plot showing *NECTIN2* and *CXCL12* expression *Z* score in macrophage subtypes.

(G) Boxplots showing the mean CD163 module score in macrophages for patients with short and long platinum free interval (PFI), separately for chemo-naive ($n$ = 10 long, $n$ = 19 short) and IDS ($n$ = 7 long, $n$ = 15 short) samples with Wilcoxon test $p$ values. Black horizontal lines represent the sample medians, boxes extend from the first to the third quartile, and whiskers equals 1.5 interquartile range.

(H) UMAP plot representation of inferred CD8$^+$ T cell subtypes.

(I) Heatmap showing *CXCR4*, *CD96*, *TIGIT*, and *CD226* expression *Z* scores in CD8$^+$ T cell subtypes.

(J) Dot plot comparing the expression of selected ligands and receptors in immune deconvoluted bulk RNA-seq data between chemo-naive ($n$ = 25) and IDS ($n$ = 25) samples with Wilcoxon test $p$ values.

(K) Overview of the linear mixed model.

(L) Heatmap summary of linear mixed modeling showing coefficients for predicting, from genetic and clinical data, changes in *CXCR4*, *NECTIN2*, *LAG3*, *CXCL12*, *CD96*, *TIGIT*, and *CD226* expression after chemotherapy on the immune compartment of deconvoluted ovarian cancer tumors ($n$ = 50). Star denotes significance in t test without multiple testing correction.

See also Figure S4 and Table S2.

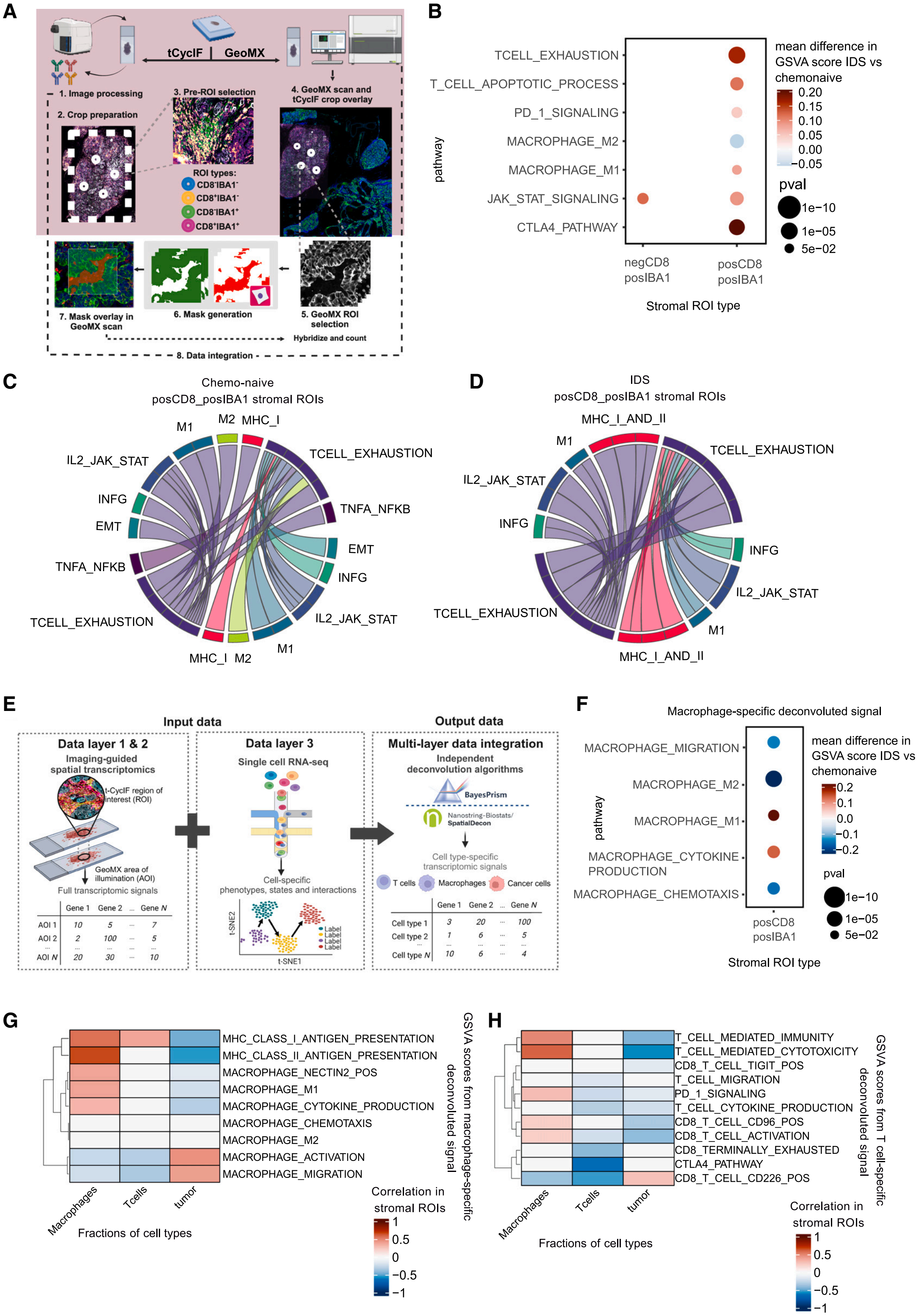

**Figure 5. GeoMx spatial transcriptomics reveals differences in pathway activities between regions of different CD8$^+$ T cell and IBA1$^+$ myeloid cell abundance**

(A) The experimental workflow for *n* = 16 samples.

(B) Dot plot representing statistically significant differences (Wilcoxon test *p* value < 0.05) between interval debulking surgery (IDS) (*n* = 111) vs. chemo-naive (*n* = 48) stromal regions of interest (ROIs), in gene set variation analysis (GSVA) scores of 19 pathways, per each AOI type.

*(legend continued on next page)*

and macrophage profiles (Tables S3 and S4; Figures S5I, S5J, and 5C, STAR Methods). Here, we found that NACT enriched M1 and reduced M2 polarization of macrophages as assessed by both scRNA-seq (Figure 5F) and literature-derived signatures[56] (Figure S5I), aligning with tCycIF analysis (Figure 5F). The M1 signature, antigen presentation, and NECTIN2$^+$ macrophage signatures correlated positively with the number of macrophages and negatively with the number of cancer cells (Figure 5G). In T cells, cytotoxicity and immunity showed strong positive correlations with the number of macrophages and negative correlations with the number of tumor cells (Figure 5H). CD96 signature correlated positively with macrophages, TIGIT and CD96 signatures negatively with tumor cells, while CD226 presented with opposite patterns (Figure 5H).

In summary, our integrative spatial transcriptomic analyses illustrate that chemotherapy drives both activated, highly antigen presenting, NECTIN2$^+$, M1-like macrophages, and cytotoxic yet exhausted and immune-checkpoint positive CD8$^+$ T cells colocalizing with macrophages within the peritumoral stroma. Moreover, the M1-like myeloid cell-driven T cell exhaustion observed within the Myelonets was corroborated at the gene expression level within the TSI. Additionally, our analysis revealed that even within the peritumoral TSI, regions containing cancer cells are depleted of NECTIN2 and its immune-checkpoint receptors, TIGIT and CD96. This further emphasizes the critical role of macrophages in spatially regulating T cell exhaustion. Interestingly, the observed opposite patterns suggest a role for CD226 in regulating the CD8$^+$ T - cancer cell interactions associated with good prognosis (Figure 2J). Our results thus reveal the transcriptional determinants of the myeloid-driven spatial T cell exhaustion, which is also associated with poor prognosis (Figure 3K).

### Targeting chemotherapy-induced TIGIT-NECTIN2 interactions with ICB enhances CD8$^+$ T cell activation

To functionally investigate whether myeloid-driven CD8$^+$ T cell exhaustion could be therapeutically targeted, we used our previously established functional immuno-oncology platform: three-dimensional patient-derived immune-competent cultures (iPDCs), which retain HGSC cancer cells and various native immune cells in a physiologically relevant matrix.[57] For this study, we generated iPDCs from 5 chemo-naive and 6 IDS patient samples and evaluated their *in vitro* responses to various ICB therapies using flow cytometry (Figure 6A). Immune cell populations in the samples were also phenotyped, confirming the presence of the relevant populations (Figures 6B and 6C). After treating iPDCs with pembrolizumab (anti-PD1 antibody) and tiragolumab (anti-TIGIT antibody) as single agents and in combination over 2–4 days, we observed significant increases in the expression of immune activation and proliferation markers, such as granzyme B and IFN-$\gamma$, and Ki67 in CD8$^+$ T cells. This was particularly pronounced in the IDS samples following treatment with pembrolizumab and/or tiragolumab (Figures 6D and S6A). We next subjected the matched tumors, from which the iPDCs were generated, to t-CycIF single-cell analysis, using antibodies also for NECTIN2 and TIGIT (Figure 6E). Supporting the findings from the single-cell and ligand-receptor analyses, we found that TIGIT expression in tumor-infiltrating CD8$^+$ T cells significantly positively correlated with the proportion of NECTIN2$^+$ myeloid cells in the tumors (Figure 6F). Importantly, we found that TIGIT expression in the CD8$^+$ T cells and the proportion of NECTIN2$^+$ myeloid cells both correlated significantly with the CD8$^+$ T cell activation after treatment with tiragolumab (Figures 6G and 6H). Similarly, CD8$^+$ T cell TIGIT expression was also associated with iPDC responses to the combination of pembrolizumab and tiragolumab (Figure 6I). These observations suggest that the spatial, macrophage-driven CD8$^+$ T cell exhaustion in HGSC can be effectively targeted with ICB, especially when administered after chemotherapy. Moreover, the benefit from these treatments appears to be intrinsically linked to the presence of NECTIN2-TIGIT signaling loop in the tumors.

## DISCUSSION

Our multi-omics study, incorporating data from two large clinical cohorts at a large single cell and spatial scale, illuminates the dynamic shifts within the TME, encompassing alterations in cell subtypes, states, spatial arrangements, and the intricate molecular and cellular interconnection in response to platinum-based chemotherapy (Figure 6J). This comprehensive approach revealed chemotherapy induced T cell infiltration and spatially confined T cell exhaustion within myeloid neighborhoods, and uncovered TIGIT-NECTIN2 interaction as a target for therapeutic interventions.

Consistent with our findings, prior studies have reported increased stromal and intraepithelial CD8$^+$ T cell infiltration following NACT.[36,58–60] Although this surge in CD8$^+$ T cells suggests a potential response to PD1/PDL1 checkpoint blockade,[61] previous studies have shown inconsistent results, likely due to concurrent immunosuppressive factors.[61] Mixed outcomes have also been observed in macrophage populations.[24,58–60] Our t-CycIF data revealed no significant changes in macrophage infiltration post-NACT. Additionally, while individual exhaustion markers were induced by chemotherapy in bulk RNA-seq data, we found that chemotherapy-induced exhaustion of tumor-recognizing CD8$^+$ T cells[63] was spatially confined within the M1-like myeloid neighborhoods.

---

(C and D) Circle plots showing groups of pathways significantly correlated (*p* value<=0.05, Spearman correlation coefficient>0.6) with the T cell exhaustion pathway group in posCD8_posIBA1 (C) chemo-naive (*n* = 32) and (D) IDS (*n* = 78) stromal ROIs. Each line represents one significantly correlated pathway from a pathway group. Each connection is shown twice—in the color of the pathway group of interest and in the color of the T cell exhaustion group.

(E) Workflow representing the integration of high-plex cyclic immunofluorescence (t-CyCIF), GeoMx, and scRNA-seq data layers to perform deconvolution of full transcriptomics GeoMx signal into cell-type specific transcriptomic profiles.

(F) Dot plots of changes in GSVA scores from deconvoluted macrophage-specific signal of 9 selected pathways representing macrophage biology between IDS (*n* = 111) vs. chemo-naive (*n* = 48) stromal regions of interest (ROIs). Dot plots show only the pathways and ROI types displaying significant differences (Wilcoxon test *p* value<0.05).

(G and H) Heatmaps representing significant (*p* value <0.05) Spearman correlation coefficient scores between GSVA scores (from deconvoluted signal) of selected pathways representing (G) macrophage and (H) T cell biology, and the fraction of key cell types within each stromal ROI (*n* = 159).

See also Figure S5 and Tables S1, S3, and S4.

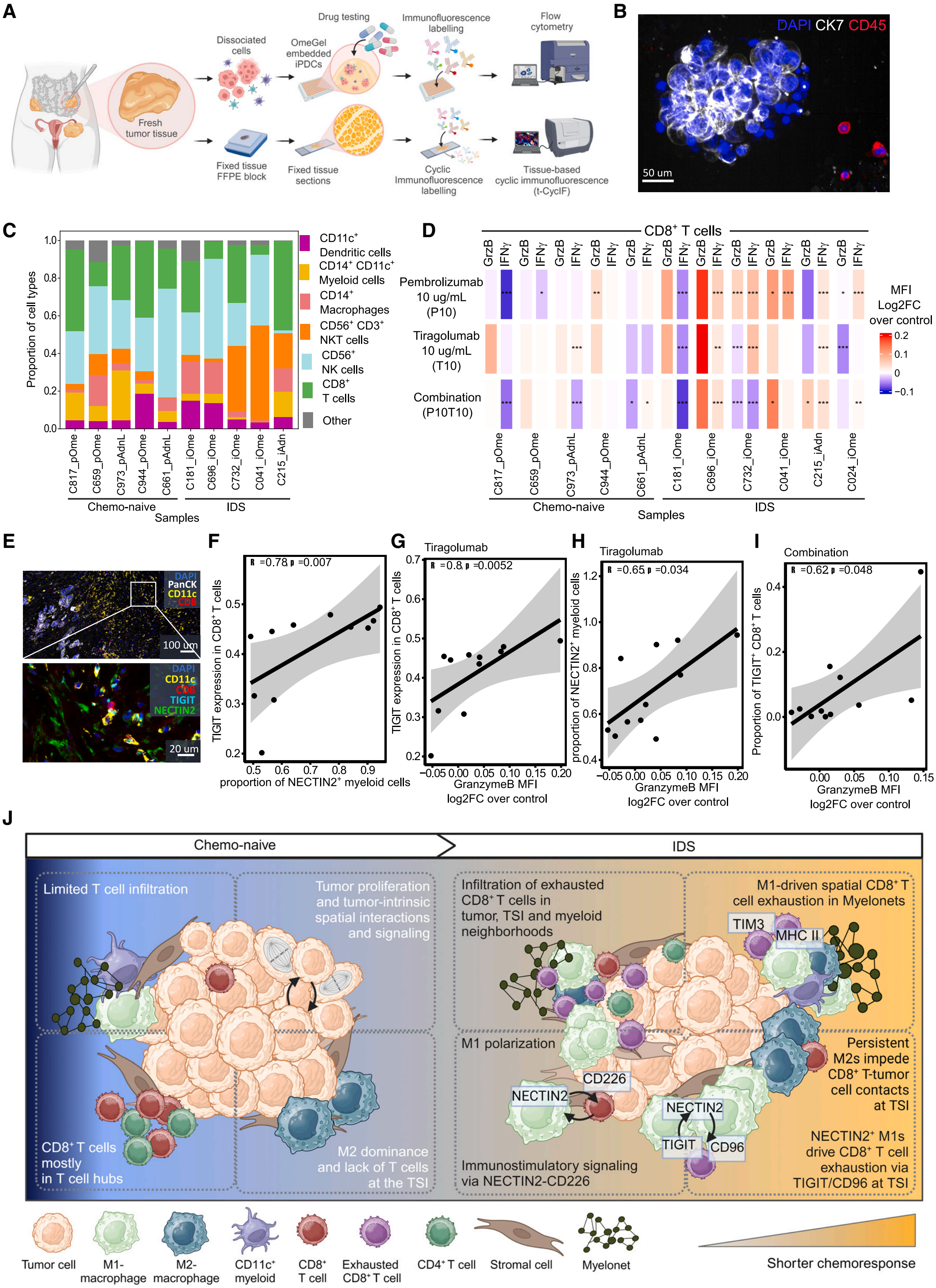

**Figure 6. Immunocompetent patient-derived cultures show T cell activation following anti-TIGIT and anti-PD1 treatments**

(A) Functional validation workflow illustrating drug testing on patient-derived immune-competent cultures (iPDCs) and high-plex cyclic immunofluorescence (t-CycIF) analysis of source tissues from the same patients ($n = 11$).

(B) Representative immunofluorescence image of iPDCs showing a cancer cell spheroid with infiltrating immune cells.

*(legend continued on next page)*

We describe Myelonets—networks of interconnected myeloid cells—as a previously uncovered spatial entity. Similarly to spatially interacting lymphocytes,[64] we show that Myelonets range from small networks to those spanning thousands of cells, which exhibit distinct functional profiles. We reveal that Myelonets are the key multicellular spatial hubs governing T cell-myeloid interactions and driving T cell exhaustion. In line with our findings, M2-polarized macrophages have been found to functionally associate with CD8$^+$ T cell exclusion,[65] while M1-polarized macrophages are crucial for effective checkpoint blockade therapies.[66] Our study substantially deepens our understanding of myeloid-driven immunosuppression in the context of chemotherapy-treated tumors. We discovered that M1-driven T cell exhaustion is localized to myelonets and peritumoral myeloid-rich regions, while M2-driven immunosuppression occurs through the direct inhibition of CD8$^+$ T cell to tumor cell contacts at the TSI, both driving poor chemoresponse. Our results suggest that patients with limited chemoresponse may benefit from ICB combination therapies targeting M1-driven exhaustion in Myelonets and M2-driven inhibition of CD8$^+$ T cell interactions[65] at TSI after NACT.

Chemotherapy distinctly induced enhanced interactions of TIGIT and CD96 in CD8$^+$ T cells with NECTIN2 in macrophages. This together with the chemotherapy-induced expression of *TIGIT* highlights the potential of targeting TIGIT in chemotherapy-treated HGSC patients. *TIGIT* has been found to be highly expressed in exhausted CD8$^+$ T cells in HGSC, and targeting TIGIT reduced tumor growth *in vivo*.[67] Further, the TIGIT-NECTIN2 axis has been found to be important in ovarian[68] and other cancer types[69,70] and phase III clinical trials targeting TIGIT are ongoing.[71,72] Consistent with findings from single-cell and spatial analyses, we observed that enhanced responses to an anti-TIGIT antibody in IDS samples was correlated with myeloid NECTIN2-CD8$^+$ T cell TIGIT signaling in the tumors, suggesting that the benefit from these treatments is embedded in the tumor ecosystem dynamics. Our results highlight the potential of targeting TIGIT and PD1 in HGSC to release exhausted CD8$^+$ T cells within myeloid niches, and uncover a tissue-based biomarker for anti-TIGIT based combination immunotherapies.

In conclusion, our findings underscore the intricate co-evolution of the tumor-immune-stromal milieu during the course of chemotherapy, exerting profound effects on niche-specific anti-tumor immunity that reveal potential therapeutic targets. Awareness of the dynamic shifts in the tumor ecosystem during standard-of-care chemotherapy is crucial for optimizing strategies that could effectively unleash CD8$^+$ T cell anti-tumor immunity in HGSC.

### Limitations of the study

In the non-randomized real-word setting of the DECIDER and Oncosys-OVA trials, for scRNA-seq, we chose to profile only IDS samples containing sufficient cancer cell content. The t-CycIF marker panel did not capture all immune cell subpopulations (e.g., myeloid-derived suppressor cells, NK cells), leaving 14% of cells unassigned. Additionally, tissue sampling from consistent anatomical sites post-chemotherapy was challenging due to treatment-induced tumor reduction. Sampling more metastatic sites during chemotherapy could further strengthen the findings.

## RESOURCE AVAILABILITY

### Lead contact

Further information and requests for resources and reagents should be directed to and will be fulfilled by the lead contact, Anniina Färkkilä (anniina.farkkila@helsinki.fi).

### Materials availability

This study did not generate new unique reagents.

### Data and code availability

- Unpublished raw scRNA-seq data have been deposited in the European Genome-phenome Archive (EGA: EGAD50000000862), and processed scRNA-seq data have been deposited in Gene Expression Omnibus (GEO: GSE266577) and are publicly available, with Table S7 indicating samples with previously published data. The raw images and quantified signals for t-CycIF data, GeoMx raw data and annotations, as well as microscopy and flow cytometry data reported in this paper have been deposited to Synapse: https://doi.org/10.7303/syn53283672. WGS and bulk RNA-seq data from the DECIDER cohort have been deposited in EGA: EGAS00001006775, EGAS00001004714. All GEO, EGA and Synapse DOIs and accession numbers are also listed in the key resources table. WES or bulk RNA-seq data from the Oncosys-OVA cohort were only used for patient-level annotations, and the raw data cannot be publicly shared due to countervailing local legal prohibition.
- All custom scripts have been deposited to Zenodo: https://doi.org/10.5281/zenodo.13849272 and are publicly available.
- Any additional information required to reanalyze the data reported in this paper is available from the lead contact upon request.

## ACKNOWLEDGMENTS

This work was supported by the European Union's Horizon 2020 research and innovation programme under grant agreement no. 667403 for HERCULES and no. 965193 for DECIDER. This study was co-funded by the European Union (ERC, SPACE 101076096 and ERC STRONGER 101125261). Views and opinions expressed are however those of the author(s) only and do not necessarily reflect those of the European Union or the European Research Council. Neither the European Union nor the granting authority can be held responsible for them.

---

(C) Bar plots presenting the proportions of different immune cell populations in the chemo-naive ($n = 5$) and interval debulking surgery (IDS) ($n = 5$) iPDCs.
(D) Heatmap illustrating the log2 fold-change of the mean fluorescence intensity (MFI) of granzyme B and IFN$\gamma$ in CD8$^+$ T cells under different treatment conditions relative to each non-treated control across different samples (chemo-naive $n = 5$, IDS $n = 6$) (Wilcoxon test; $^*p < 0.05$, $^{**}p < 0.01$, $^{***}p < 0.001$).
(E) Representative t-CycIF image showing NECTIN2-TIGIT interactions.
(F–I) Scatterplots from t-CycIF data ($n = 11$ patients) showing (F) median TIGIT expression in CD8$^+$ T cells and the proportion of NECTIN2$^+$ myeloid cells, (G) median TIGIT expression from the source tumor and respective granzyme B MFI log2FC in the tiragolumab treatment setting, (H) the proportion of NECTIN2$^+$ myeloid cells in the source tumor and respective granzyme B MFI log2FC in the tiragolumab treatment setting and (I) the proportion of TIGIT$^+$CD8$^+$ T cells from the source tumor and respective granzyme B MFI log2FC in the combination treatment setting. Black line represents a fitted linear model with confidence intervals as gray areas, with its R and $p$ value parameters for Spearman correlation.
(J) Summary figure highlighting the differences between chemo-naive and IDS samples.
See also Figure S6.

Funding was also received from the Sigrid Jusélius Foundation, Research Council of Finland (1339805 and 350396), Cancer Foundation Finland, Finnish Medical, Ida Montini Emil Aaltonen, Biomedicum, K. Albin Johanssons, and Instrumentarium Foundations, Finland, and HORIZON-MSCA-2021- PF, European Commission (M.M.F.: 101067835), Ludwig Cancer Research Center at Harvard Medical School (P.K.S) and R00CA256497 (A.J.N.) from NCI. The authors thank the CSC – IT Center for Science for computational resources and the FIMM-HCA and Genomics units, and FIMM SCA unit supported by HiLIFE and Biocenter FInland for their services.

Figures 1A, 5A, 5E, 6A, and 6J were created with Biorender.com.

We are grateful to Dr. Yafei Wang and Ziqi Kang for proofreading the manuscript, Saundarya Shah, Anni Härkönen, and Anni Suoknuuti for data curation, and MD Lasse Suominen for CAF analysis for the review.

## AUTHOR CONTRIBUTIONS

I.-M.L. designed, processed, and analyzed t-CyCIF data and wrote the manuscript. I.N. designed, generated, and analyzed GeoMx data and wrote the manuscript. M.H.-O. designed and performed iPDC experiments, analyzed the data, and wrote the manuscript. E.P.E. generated, processed, and analyzed scRNA-seq data and wrote the manuscript. A.S. preprocessed t-CyCIF data. A.N. helped with iPDC models. D.A. analyzed RNAseq data and wrote the manuscript. A.J. performed GeoMx experiments, Z.L. assisted with GeoMX data analyses. M.M.F. preprocessed scRNA-seq data and built the linear-mixed model. F.P.-V. and J.O. analyzed genomic data. M.S., U.-M.H., E.K., A.V., and J.H. provided samples and clinical data. T.V. and A.J.N. supported the data analysis. S.H. and P.K.S. supported the data analysis and provided resources. A.V. and A.F. conceived and supervised the study and wrote the manuscript.

## DECLARATION OF INTERESTS

P.K.S. is a co-founder and member of the BOD of Glencoe Software, is a member of the SAB for RareCyte, Nanostring, Reverb Therapeutics and Montai Health, and consults for Merck; he holds equity in Glencoe and RareCyte.

## STAR★METHODS

Detailed methods are provided in the online version of this paper and include the following:

- KEY RESOURCES TABLE
- EXPERIMENTAL MODEL AND STUDY PARTICIPANT DETAILS
  - ○ Cohort description
- METHOD DETAILS
  - ○ Highplex t-CyCIF imaging and image processing
  - ○ t-CyCIF cell phenotyping
  - ○ t-CycIF spatial analysis
  - ○ Low-plex t-CyCIF staining and image processing
  - ○ Low-plex t-CyCIF cell type calling
  - ○ Sample preparation for scRNA-seq
  - ○ Preprocessing scRNA-seq data
  - ○ Cell type annotation in scRNA-seq data
  - ○ Identifying macrophage states in scRNA-seq data
  - ○ Identifying CD8$^+$ T cell states in scRNA-seq data
  - ○ Differential cell abundance analysis in scRNA-seq data
  - ○ Ligand-receptor interaction analysis
  - ○ Pathway activity inference in scRNA-seq data
  - ○ Linear mixed models
  - ○ Quantification of T cell exhaustion in scRNA-seq data
  - ○ GeoMx
  - ○ GeoMx ROI selection with lowplex t-CyCIF crop overlay
  - ○ GeoMx and t-CyCIF data pairing
  - ○ GeoMx data quality control and preprocessing
  - ○ GeoMx pathway activity analysis and correlation analysis on the full transcriptomics signal
  - ○ GeoMx signal deconvolution
  - ○ GeoMx pathway activity analysis and correlation analysis on the deconvoluted transcriptomic signal
  - ○ WGS and SBS3
  - ○ Genomic homologous recombination deficiency scoring
  - ○ Bulk RNA-seq data analysis
  - ○ iPDCs generation and drug testing
- QUANTIFICATION AND STATISTICAL ANALYSIS

## SUPPLEMENTAL INFORMATION

Supplemental information can be found online at https://doi.org/10.1016/j.ccell.2024.11.005.

Received: March 18, 2024
Revised: August 30, 2024
Accepted: November 7, 2024
Published: November 28, 2024

## REFERENCES

1. Chow, A., Perica, K., Klebanoff, C.A., and Wolchok, J.D. (2022). Clinical implications of T cell exhaustion for cancer immunotherapy. Nat. Rev. Clin. Oncol. *19*, 775–790.
2. Robert, C., Schachter, J., Long, G.V., Arance, A., Grob, J.J., Mortier, L., Daud, A., Carlino, M.S., McNeil, C., Lotem, M., et al. (2015). Pembrolizumab versus Ipilimumab in Advanced Melanoma. N. Engl. J. Med. *372*, 2521–2532.
3. Robert, C. (2020). A decade of immune-checkpoint inhibitors in cancer therapy. Nat. Commun. *11*, 3801.
4. Matulonis, U.A., Shapira-Frommer, R., Santin, A.D., Lisyanskaya, A.S., Pignata, S., Vergote, I., Raspagliesi, F., Sonke, G.S., Birrer, M., Provencher, D.M., et al. (2019). Antitumor activity and safety of pembrolizumab in patients with advanced recurrent ovarian cancer: results from the phase II KEYNOTE-100 study. Ann. Oncol. *30*, 1080–1087.
5. Pujade-Lauraine, E., Fujiwara, K., Ledermann, J.A., Oza, A.M., Kristeleit, R., Ray-Coquard, I.-L., Richardson, G.E., Sessa, C., Yonemori, K., Banerjee, S., et al. (2021). Avelumab alone or in combination with chemotherapy versus chemotherapy alone in platinum-resistant or platinum-refractory ovarian cancer (JAVELIN Ovarian 200): an open-label, three-arm, randomised, phase 3 study. Lancet Oncol. *22*, 1034–1046.
6. Moore, K.N., Bookman, M., Sehouli, J., Miller, A., Anderson, C., Scambia, G., Myers, T., Taskiran, C., Robison, K., Mäenpää, J., et al. (2021). Atezolizumab, Bevacizumab, and Chemotherapy for Newly Diagnosed Stage III or IV Ovarian Cancer: Placebo-Controlled Randomized Phase III Trial (IMagyn050/GOG 3015/ENGOT-OV39). J. Clin. Oncol. *39*, 1842–1855.
7. Monk, B.J., Colombo, N., Oza, A.M., Fujiwara, K., Birrer, M.J., Randall, L., Poddubskaya, E.V., Scambia, G., Shparyk, Y.V., Lim, M.C., et al. (2021). Chemotherapy with or without avelumab followed by avelumab maintenance versus chemotherapy alone in patients with previously untreated epithelial ovarian cancer (JAVELIN Ovarian 100): an open-label, randomised, phase 3 trial. Lancet Oncol. *22*, 1275–1289.
8. Cancer Genome Atlas Research Network (2011). Integrated genomic analyses of ovarian carcinoma. Nature *474*, 609–615.
9. Yeung, T.-L., Leung, C.S., Yip, K.-P., Au Yeung, C.L., Wong, S.T.C., and Mok, S.C. (2015). Cellular and molecular processes in ovarian cancer metastasis. A Review in the Theme: Cell and Molecular Processes in Cancer Metastasis. Am. J. Physiol. Cell Physiol. *309*, C444–C456.
10. Lahtinen, A., Lavikka, K., Virtanen, A., Li, Y., Jamalzadeh, S., Skorda, A., Lauridsen, A.R., Zhang, K., Marchi, G., Isoviita, V.-M., et al. (2023). Evolutionary states and trajectories characterized by distinct pathways stratify patients with ovarian high grade serous carcinoma. Cancer Cell *41*, 1103–1117.e12.
11. Smith, P., Bradley, T., Gavarró, L.M., Goranova, T., Ennis, D.P., Mirza, H.B., De Silva, D., Piskorz, A.M., Sauer, C.M., Al-Khalidi, S., et al.

(2023). The copy number and mutational landscape of recurrent ovarian high- grade serous carcinoma. Nat. Commun. *14*, 4387.

12. Wright, A.A., Bohlke, K., Armstrong, D.K., Bookman, M.A., Cliby, W.A., Coleman, R.L., Dizon, D.S., Kash, J.J., Meyer, L.A., Moore, K.N., et al. (2016). Neoadjuvant chemotherapy for newly diagnosed, advanced ovarian cancer: Society of Gynecologic Oncology and American Society of Clinical Oncology Clinical Practice Guideline. Gynecol. Oncol. *143*, 3–15.
13. Colombo, N., Sessa, C., du Bois, A., Ledermann, J., McCluggage, W.G., McNeish, I., Morice, P., Pignata, S., Ray-Coquard, I., Vergote, I., et al. (2019). ESMO-ESGO consensus conference recommendations on ovarian cancer: pathology and molecular biology, early and advanced stages, borderline tumours and recurrent disease. Ann. Oncol. *30*, 672–705.
14. Kemp, Z., and Ledermann, J. (2013). Update on first-line treatment of advanced ovarian carcinoma. Int. J. Womens Health *5*, 45–51.
15. Launonen, I.-M., Lyytikäinen, N., Casado, J., Anttila, E.A., Szabó, A., Haltia, U.-M., Jacobson, C.A., Lin, J.R., Maliga, Z., Howitt, B.E., et al. (2022). Single-cell tumor-immune microenvironment of BRCA1/2 mutated high-grade serous ovarian cancer. Nat. Commun. *13*, 835.
16. Färkkilä, A., Gulhan, D.C., Casado, J., Jacobson, C.A., Nguyen, H., Kochupurakkal, B., Maliga, Z., Yapp, C., Chen, Y.-A., Schapiro, D., et al. (2020). Immunogenomic profiling determines responses to combined PARP and PD-1 inhibition in ovarian cancer. Nat. Commun. *11*, 1459.
17. Li, J., Wang, J., Chen, R., Bai, Y., and Lu, X. (2017). The prognostic value of tumor-infiltrating T lymphocytes in ovarian cancer. Oncotarget *8*, 15621–15631.
18. Yuan, X., Zhang, J., Li, D., Mao, Y., Mo, F., Du, W., and Ma, X. (2017). Prognostic significance of tumor- associated macrophages in ovarian cancer: A meta-analysis. Gynecol. Oncol. *147*, 181–187.
19. Zhang, L., Conejo-Garcia, J.R., Katsaros, D., Gimotty, P.A., Massobrio, M., Regnani, G., Makrigiannakis, A., Gray, H., Schlienger, K., Liebman, M.N., et al. (2003). Intratumoral T cells, recurrence, and survival in epithelial ovarian cancer. N. Engl. J. Med. *348*, 203–213.
20. Ovarian Tumor Tissue Analysis (OTTA) Consortium, Goode, E.L., Block, M.S., Kalli, K.R., Vierkant, R.A., Chen, W., Fogarty, Z.C., Gentry-Maharaj, A., Tołoczko, A., Hein, A., et al. (2017). Dose-Response Association of CD8+ Tumor-Infiltrating Lymphocytes and Survival Time in High-Grade Serous Ovarian Cancer. JAMA Oncol. *3*, e173290.
21. Zhang, K., Erkan, E.P., Jamalzadeh, S., Dai, J., Andersson, N., Kaipio, K., Lamminen, T., Mansuri, N., Huhtinen, K., Carpén, O., et al. (2022). Longitudinal single-cell RNA-seq analysis reveals stress-promoted chemoresistance in metastatic ovarian cancer. Sci. Adv. *8*, eabm1831.
22. Jiménez-Sánchez, A., Cybulska, P., Mager, K.L., Koplev, S., Cast, O., Couturier, D.-L., Memon, D., Selenica, P., Nikolovski, I., Mazaheri, Y., et al. (2020). Unraveling tumor-immune heterogeneity in advanced ovarian cancer uncovers immunogenic effect of chemotherapy. Nat. Genet. *52*, 582–593.
23. Böhm, S., Montfort, A., Pearce, O.M.T., Topping, J., Chakravarty, P., Everitt, G.L.A., Clear, A., McDermott, J.R., Ennis, D., Dowe, T., et al. (2016). Neoadjuvant Chemotherapy Modulates the Immune Microenvironment in Metastases of Tubo-Ovarian High-Grade Serous Carcinoma. Clin. Cancer Res. *22*, 3025–3036.
24. Heath, O., Berlato, C., Maniati, E., Lakhani, A., Pegrum, C., Kotantaki, P., Elorbany, S., Böhm, S., Barry, S.T., Annibaldi, A., et al. (2021). Chemotherapy Induces Tumor-Associated Macrophages that Aid Adaptive Immune Responses in Ovarian Cancer. Cancer Immunol. Res. *9*, 665–681.
25. Lin, J.-R., Fallahi-Sichani, M., and Sorger, P.K. (2015). Highly multiplexed imaging of single cells using a high- throughput cyclic immunofluorescence method. Nat. Commun. *6*, 8390.
26. Giesen, C., Wang, H.A.O., Schapiro, D., Zivanovic, N., Jacobs, A., Hattendorf, B., Schüffler, P.J., Grolimund, D., Buhmann, J.M., Brandt, S., et al. (2014). Highly multiplexed imaging of tumor tissues with subcellular resolution by mass cytometry. Nat. Methods *11*, 417–422.
27. Duraiswamy, J., Turrini, R., Minasyan, A., Barras, D., Crespo, I., Grimm, A.J., Casado, J., Genolet, R., Benedetti, F., Wicky, A., et al. (2021). Myeloid antigen-presenting cell niches sustain antitumor T cells and license PD-1 blockade via CD28 costimulation. Cancer Cell *39*, 1623–1642.e20.
28. Wang, X.Q., Danenberg, E., Huang, C.-S., Egle, D., Callari, M., Bermejo, B., Dugo, M., Zamagni, C., Thill, M., Anton, A., et al. (2023). Spatial predictors of immunotherapy response in triple-negative breast cancer. Nature *621*, 868–876.
29. Nirmal, A.J., Maliga, Z., Vallius, T., Quattrochi, B., Chen, A.A., Jacobson, C.A., Pelletier, R.J., Yapp, C., Arias- Camison, R., Chen, Y.-A., et al. (2022). The Spatial Landscape of Progression and Immunoediting in Primary Melanoma at Single-Cell Resolution. Cancer Discov. *12*, 1518–1541.
30. Schürch, C.M., Bhate, S.S., Barlow, G.L., Phillips, D.J., Noti, L., Zlobec, I., Chu, P., Black, S., Demeter, J., McIlwain, D.R., et al. (2020). Coordinated Cellular Neighborhoods Orchestrate Antitumoral Immunity at the Colorectal Cancer Invasive Front. Cell *183*, 838.
31. Golstein, P., and Griffiths, G.M. (2018). An early history of T cell-mediated cytotoxicity. Nat. Rev. Immunol. *18*, 527–535.
32. Larroquette, M., Guegan, J.-P., Besse, B., Cousin, S., Brunet, M., Le Moulec, S., Le Loarer, F., Rey, C., Soria, J.-C., Barlesi, F., et al. (2022). Spatial transcriptomics of macrophage infiltration in non-small cell lung cancer reveals determinants of sensitivity and resistance to anti-PD1/PD-L1 antibodies. J. Immunother. Cancer *10*, e003890. https://doi.org/10.1136/jitc-2021-003890.
33. Pardoll, D.M. (2012). The blockade of immune checkpoints in cancer immunotherapy. Nat. Rev. Cancer *12*, 252–264.
34. Kang, Z., Szabo, A., Farago, T., Perez-Villatoro, F., Launonen, I.-M., Anttila, E., Elias, K., Casado, J., Sorger, P., and Färkkilä, A. (2024). Tribus: Semi-automated discovery of cell identities and phenotypes from multiplexed imaging and proteomic data. Preprint at bioRxiv. https://doi.org/10.1101/2024.03.13.584767.
35. Domínguez Conde, C., Xu, C., Jarvis, L.B., Rainbow, D.B., Wells, S.B., Gomes, T., Howlett, S.K., Suchanek, O., Polanski, K., King, H.W., et al. (2022). Cross-tissue immune cell analysis reveals tissue-specific features in humans. Science *376*, eabl5197.
36. Leary, A., Genestie, C., Blanc-Durand, F., Gouy, S., Dunant, A., Maulard, A., Drusch, F., Cheaib, B., Michels, J., Bentivegna, E., et al. (2021). Neoadjuvant chemotherapy alters the balance of effector to suppressor immune cells in advanced ovarian cancer. Cancer Immunol. Immunother. *70*, 519–531.
37. Rao, C. (1982). Diversity and dissimilarity coefficients: A unified approach. Theor. Popul. Biol. *21*, 24–43.
38. Shen, W., Wang, X., Xiang, H., Shichi, S., Nakamoto, H., Kimura, S., Sugiyama, K., Taketomi, A., and Kitamura, H. (2023). IFN-γ-STAT1-mediated NK2R expression is involved in the induction of antitumor effector CD8+ T cells *in vivo*. Cancer Sci. *114*, 1816–1829.
39. Michie, C.A., McLean, A., Alcock, C., and Beverley, P.C. (1992). Lifespan of human lymphocyte subsets defined by CD45 isoforms. Nature *360*, 264–265.
40. Wang, T., Wang, Z., Niu, R., and Wang, L. (2019). Crucial role of Anxa2 in cancer progression: highlights on its novel regulatory mechanism. Cancer Biol. Med. *16*, 671–687.
41. Kim, D.-H., Kang, Y.N., Jin, J., Park, M., Kim, D., Yoon, G., Yun, J.W., Lee, J., Park, S.Y., Lee, Y.R., et al. (2024). Glutamine-derived aspartate is required for eIF5A hypusination-mediated translation of HIF-ϭŋ łŽ ŝŶĔŽĐĞ the polarization of tumor-associated macrophages. Exp. Mol. Med. *56*, 1123–1136.
42. Dann, E., Henderson, N.C., Teichmann, S.A., Morgan, M.D., and Marioni, J.C. (2022). Differential abundance testing on single-cell data using k-nearest neighbor graphs. Nat. Biotechnol. *40*, 245–253.

43. Browaeys, R., Gilis, J., Sang-Aram, C., De Bleser, P., Hoste, L., Tavernier, S., Lambrechts, D., Seurinck, R., and Saeys, Y. (2023). MultiNicheNet: a flexible framework for differential cell-cell communication analysis from multi-sample multi-condition single-cell transcriptomics data. Preprint at bioRxiv. https://doi.org/10.1101/2023.06.13.544751.

44. Braun, M., Aguilera, A.R., Sundarrajan, A., Corvino, D., Stannard, K., Krumeich, S., Das, I., Lima, L.G., Meza Guzman, L.G., Li, K., et al. (2020). CD155 on Tumor Cells Drives Resistance to Immunotherapy by Inducing the Degradation of the Activating Receptor CD226 in CD8 T Cells. Immunity *53*, 805–823.e15.

45. Weulersse, M., Asrir, A., Pichler, A.C., Lemaitre, L., Braun, M., Carrié, N., Joubert, M.-V., Le Moine, M., Do Souto, L., Gaud, G., et al. (2020). Eomes-Dependent Loss of the Co-activating Receptor CD226 Restrains CD8 T Cell Anti-tumor Functions and Limits the Efficacy of Cancer Immunotherapy. Immunity *53*, 824–839.e10.

46. Maruhashi, T., Okazaki, I.-M., Sugiura, D., Takahashi, S., Maeda, T.K., Shimizu, K., and Okazaki, T. (2018). LAG-3 inhibits the activation of CD4 T cells that recognize stable pMHCII through its conformation-dependent recognition of pMHCII. Nat. Immunol. *19*, 1415–1426.

47. Woo, S.-R., Turnis, M.E., Goldberg, M.V., Bankoti, J., Selby, M., Nirschl, C.J., Bettini, M.L., Gravano, D.M., Vogel, P., Liu, C.L., et al. (2012). Immune inhibitory molecules LAG-3 and PD-1 synergistically regulate T-cell function to promote tumoral immune escape. Cancer Res. *72*, 917–927.

48. Andreatta, M., Corria-Osorio, J., Müller, S., Cubas, R., Coukos, G., and Carmona, S.J. (2021). Interpretation of T cell states from single-cell transcriptomics data using reference atlases. Nat. Commun. *12*, 1–19.

49. Morotti, M., Grimm, A.J., Hope, H.C., Arnaud, M., Desbuisson, M., Rayroux, N., Barras, D., Masid, M., Murgues, B., Chap, B.S., et al. (2024). PGE inhibits TIL expansion by disrupting IL-2 signalling and mitochondrial function. Nature *629*, 426–434.

50. Lacher, S.B., Dörr, J., de Almeida, G.P., Hönninger, J., Bayerl, F., Hirschberger, A., Pedde, A.-M., Meiser, P., Ramsauer, L., Rudolph, T.J., et al. (2024). PGE limits effector expansion of tumour-infiltrating stem-like CD8 T cells. Nature *629*, 417–425.

51. Häkkinen, A., Zhang, K., Alkodsi, A., Andersson, N., Erkan, E.P., Dai, J., Kaipio, K., Lamminen, T., Mansuri, N., Huhtinen, K., et al. (2021). PRISM: recovering cell-type-specific expression profiles from individual composite RNA-seq samples. Bioinformatics *37*, 2882–2888.

52. Gebhardt, T., Park, S.L., and Parish, I.A. (2023). Stem-like exhausted and memory CD8+ T cells in cancer. Nat. Rev. Cancer *23*, 780–798.

53. Ada Junquera-Mencia (2023). University of Helsinki Translational Medicine (TRANSMED). Master's thesis. http://urn.fi/URN:NBN:fi:hulib-202306142832.

54. Tur, J., Farrera, C., Sánchez-Tilló, E., Vico, T., Guerrero-Gonzalez, P., Fernandez-Elorduy, A., Lloberas, J., and Celada, A. (2021). Induction of CIITA by IFN-$\gamma$ in in macrophages involves STAT1 activation by JAK and JNK. Immunobiology *226*, 152114.

55. Chu, T., Wang, Z., Pe'er, D., and Danko, C.G. (2022). Cell type and gene expression deconvolution with BayesPrism enables Bayesian integrative analysis across bulk and single-cell RNA sequencing in oncology. Nat. Cancer *3*, 505–517.

56. Martinez, F.O., Gordon, S., Locati, M., and Mantovani, A. (2006). Transcriptional profiling of the human monocyte-to-macrophage differentiation and polarization: new molecules and patterns of gene expression. J. Immunol. *177*, 7303–7311.

57. Nagaraj, A.S., Salko, M., Sirsikar, A., Erkan, E.P., Pietilä, E.A., Niemiec, I., Bao, J., Marchi, G., Szabó, A., Nowlan, K., et al. (2024). Patient-derived functional immuno-oncology platform identifies responders to ATR inhibitor and immunotherapy combinations in ovarian cancer. Preprint at bioRxiv. https://doi.org/10.1101/2024.02.15.579904.

58. Lo, C.S., Sanii, S., Kroeger, D.R., Milne, K., Talhouk, A., Chiu, D.S., Rahimi, K., Shaw, P.A., Clarke, B.A., and Nelson, B.H. (2017). Neoadjuvant Chemotherapy of Ovarian Cancer Results in Three Patterns of Tumor- Infiltrating Lymphocyte Response with Distinct Implications for Immunotherapy. Clin. Cancer Res. *23*, 925–934.

59. Cao, G., Hua, D., Li, J., Zhang, X., Zhang, Z., Zhang, B., Bei, T., Cui, L., Chen, S., Wang, S., and Zhu, L. (2023). Tumor immune microenvironment changes are associated with response to neoadjuvant chemotherapy and long- term survival benefits in advanced epithelial ovarian cancer: A pilot study. Front. Immunol. *14*, 1022942.

60. Lodewijk, I., Bernardini, A., Suárez-Cabrera, C., Bernal, E., Sánchez, R., Garcia, J.L., Rojas, K., Morales, L., Wang, S., Han, X., et al. (2022). Genomic landscape and immune-related gene expression profiling of epithelial ovarian cancer after neoadjuvant chemotherapy. npj Precis. Oncol. *6*, 7.

61. Kandalaft, L.E., Dangaj Laniti, D., and Coukos, G. (2022). Immunobiology of high-grade serous ovarian cancer: lessons for clinical translation. Nat. Rev. Cancer *22*, 640–656.

62. Zheng, L., Qin, S., Si, W., Wang, A., Xing, B., Gao, R., Ren, X., Wang, L., Wu, X., Zhang, J., et al. (2021). Pan- cancer single-cell landscape of tumor-infiltrating T cells. Science *374*, abe6474.

63. Meier, S.L., Satpathy, A.T., and Wells, D.K. (2022). Bystander T cells in cancer immunology and therapy. Nat. Cancer *3*, 143–155.

64. Gaglia, G., Burger, M.L., Ritch, C.C., Rammos, D., Dai, Y., Crossland, G.E., Tavana, S.Z., Warchol, S., Jaeger, A.M., Naranjo, S., et al. (2023). Lymphocyte networks are dynamic cellular communities in the immunoregulatory landscape of lung adenocarcinoma. Cancer Cell *41*, 871–886.e10.

65. Peranzoni, E., Lemoine, J., Vimeux, L., Feuillet, V., Barrin, S., Kantari-Mimoun, C., Bercovici, N., Guérin, M., Biton, J., Ouakrim, H., et al. (2018). Macrophages impede CD8 T cells from reaching tumor cells and limit the efficacy of anti-PD-1 treatment. Proc. Natl. Acad. Sci. USA *115*, E4041–E4050.

66. van Elsas, M.J., Middelburg, J., Labrie, C., Roelands, J., Schaap, G., Sluijter, M., Tonea, R., Ovcinnikovs, V., Lloyd, K., Schuurman, J., et al. (2024). Immunotherapy-activated T cells recruit and skew late-stage activated M1-like macrophages that are critical for therapeutic efficacy. Cancer Cell *42*, 1032–1050.e10.

67. Xu, J., Fang, Y., Chen, K., Li, S., Tang, S., Ren, Y., Cen, Y., Fei, W., Zhang, B., Shen, Y., and Lu, W. (2022). Single-Cell RNA Sequencing Reveals the Tissue Architecture in Human High-Grade Serous Ovarian Cancer. Clin. Cancer Res. *28*, 3590–3602.

68. Chai, C., Liang, L., Wang, W., Zhao, W., Sun, C., Lin, L., Li, H., Wang, F., and Luo, Y. (2023). Single cell analysis of epithelial, immune, and stromal signatures and interactions in human ovarian cancer.

69. Wienke, J., Visser, L.L., Kholosy, W.M., Keller, K.M., Barisa, M., Munnings-Tomes, S., Carlton, E., Poon, E., Rodriguez, A., Bernardi, R., et al. (2022). Integrative analysis of neuroblastoma by single-cell RNA sequencing identifies the NECTIN2-TIGIT axis as a target for immunotherapy. Preprint at bioRxiv. https://doi.org/10.1101/2022.07.15.499859.

70. Ge, Z., Zhou, G., Campos Carrascosa, L., Gausvik, E., Boor, P.P.C., Noordam, L., Doukas, M., Polak, W.G., Terkivatan, T., Pan, Q., et al. (2021). TIGIT and PD1 Co-blockade Restores ex vivo Functions of Human Tumor-Infiltrating CD8$^{+}$ T Cells in Hepatocellular Carcinoma. Cell. Mol. Gastroenterol. Hepatol. *12*, 443–464.

71. Cho, B.C., Abreu, D.R., Hussein, M., Cobo, M., Patel, A.J., Secen, N., Lee, K.H., Massuti, B., Hiret, S., Yang, J.C.H., et al. (2022). Tiragolumab plus atezolizumab versus placebo plus atezolizumab as a first-line treatment for PD-L1-selected non-small-cell lung cancer (CITYSCAPE): primary and follow-up analyses of a randomised, double-blind, phase 2 study. Lancet Oncol. *23*, 781–792.

72. Long, G.V., Eggermont, A.M., Gershenwald, J.E., Schadendorf, D., Ascierto, P.A., Dummer, R., Hauschild, A., Carlino, M.S., Ribas, A., Robert, C., et al. (2023). KEYVIBE-010: Adjuvant coformulated vibostolimab with pembrolizumab versus adjuvant pembrolizumab in patients with high-risk stage II-IV melanoma. J. Clin. Orthod. *41*, TPS9611.

73. Dockery, L.E., Rubenstein, A.R., Ding, K., Mashburn, S.G., Burkett, W.C., Davis, A.M., Doo, D.W., Arend, R.C., Moore, K.N., and Gunderson, C.C.

(2019). Extending the platinum-free interval: The impact of omitting 2nd line platinum chemotherapy in intermediate platinum-sensitive ovarian cancer. Gynecol. Oncol. *155*, 201–206.

74. Hippen, A.A., Falco, M.M., Weber, L.M., Erkan, E.P., Zhang, K., Doherty, J.A., Vähärautio, A., Greene, C.S., and Hicks, S.C. (2021). miQC: An adaptive probabilistic framework for quality control of single-cell RNA-sequencing data. PLoS Comput. Biol. *17*, e1009290.
75. Koskela, H., Li, Y., Joutsiniemi, T., Muranen, T., Isoviita, V.-M., Huhtinen, K., Micoli, G., Lavikka, K., Marchi, G., Hietanen, S., et al. (2024). HRD related signature 3 predicts clinical outcome in advanced tubo-ovarian high-grade serous carcinoma. Gynecol. Oncol. *180*, 91–98.
76. Pikkusaari, S., Tumiati, M., Virtanen, A., Oikkonen, J., Li, Y., Perez-Villatoro, F., Muranen, T., Salko, M., Huhtinen, K., Kanerva, A., et al. (2023). Functional Homologous Recombination Assay on FFPE Specimens of Advanced High-Grade Serous Ovarian Cancer Predicts Clinical Outcomes. Clin. Cancer Res. *29*, 3110–3123.
77. Perez-Villatoro, F., Oikkonen, J., Casado, J., Chernenko, A., Gulhan, D.C., Tumiati, M., Li, Y., Lavikka, K., Hietanen, S., Hynninen, J., et al. (2022). Optimized detection of homologous recombination deficiency improves the prediction of clinical outcomes in cancer. npj Precis. Oncol. *6*, 96.
78. Jamalzadeh, S., Dai, J., Lavikka, K., Li, Y., Jiang, J., Huhtinen, K., Virtanen, A., Oikkonen, J., Hietanen, S., Hynninen, J., et al. (2024). Genome-wide quantification of copy-number aberration impact on gene expression in ovarian high-grade serous carcinoma. BMC Cancer *24*, 173.
79. Lin, J.-R., Izar, B., Wang, S., Yapp, C., Mei, S., Shah, P.M., Santagata, S., and Sorger, P.K. (2018). Highly multiplexed immunofluorescence imaging of human tissues and tumors using t-CyCIF and conventional optical microscopes. Elife *7*, e31657. https://doi.org/10.7554/eLife.31657.
80. Muhlich, J.L., Chen, Y.-A., Yapp, C., Russell, D., Santagata, S., and Sorger, P.K. (2022). Stitching and registering highly multiplexed whole-slide images of tissues and tumors using ASHLAR. Bioinformatics *38*, 4613–4621.
81. Ronneberger, O., Fischer, P., and Brox, T. (2015). U-net: Convolutional Networks for Biomedical Image Segmentation. In Medical Image Computing and Computer-Assisted Intervention – MICCAI 2015 (Springer International Publishing), pp. 234–241.
82. Dries, R., Zhu, Q., Dong, R., Eng, C.-H.L., Li, H., Liu, K., Fu, Y., Zhao, T., Sarkar, A., Bao, F., et al. (2021). Giotto: a toolbox for integrative analysis and visualization of spatial expression data. Genome Biol. *22*, 78.
83. Baddeley, A., Rubak, E., and Turner, R. (2015). Spatial Point Patterns: Methodology and Applications with R (CRC Press).
84. Debastiani, V.J., and Pillar, V.D. (2012). SYNCSA—R tool for analysis of metacommunities based on functional traits and phylogeny of the community components. Bioinformatics *28*, 2067–2068.
85. Palla, G., Spitzer, H., Klein, M., Fischer, D., Schaar, A.C., Kuemmerle, L.B., Rybakov, S., Ibarra, I.L., Holmberg, O., Virshup, I., et al. (2022). Squidpy: a scalable framework for spatial omics analysis. Nat. Methods *19*, 171–178.
86. Weigert, M., Schmidt, U., Haase, R., Sugawara, K., and Myers, G. (2019). Star-convex polyhedra for 3D object detection and segmentation in microscopy. Preprint at arXiv. https://doi.org/10.48550/arXiv.1908.03636.
87. Schmidt, U., Weigert, M., Broaddus, C., and Myers, G. (2018). Cell Detection with Star-Convex Polygons. In Medical Image Computing and Computer Assisted Intervention – MICCAI 2018 (Springer International Publishing), pp. 265–273.
88. Hao, Y., Hao, S., Andersen-Nissen, E., Mauck, W.M., Zheng, S., Butler, A., Lee, M.J., Wilk, A.J., Darby, C., Zager, M., et al. (2021). Integrated analysis of multimodal single-cell data. Cell *184*, 3573–3587.e29.
89. Stuart, T., Butler, A., Hoffman, P., Hafemeister, C., Papalexi, E., Mauck, W.M., 3rd, Hao, Y., Stoeckius, M., Smibert, P., and Satija, R. (2019). Comprehensive Integration of Single-Cell Data. Cell *177*, 1888–1902.e21.
90. Phipson, B., Sim, C.B., Porrello, E.R., Hewitt, A.W., Powell, J., and Oshlack, A. (2022). propeller: testing for differences in cell type proportions in single cell data. Bioinformatics *38*, 4720–4726.
91. Yi, H., Plotkin, A., and Stanley, N. (2024). Benchmarking differential abundance methods for finding condition-specific prototypical cells in multi-sample single-cell datasets. Genome Biol. *25*, 9.
92. Wu, T., Hu, E., Xu, S., Chen, M., Guo, P., Dai, Z., Feng, T., Zhou, L., Tang, W., Zhan, L., et al. (2021). clusterProfiler 4.0: A universal enrichment tool for interpreting omics data. Innovation *2*, 100141.
93. Yu, G., Wang, L.-G., Han, Y., and He, Q.-Y. (2012). clusterProfiler: an R package for comparing biological themes among gene clusters. OMICS *16*, 284–287.
94. Badia-I-Mompel, P., Vélez Santiago, J., Braunger, J., Geiss, C., Dimitrov, D., Müller-Dott, S., Taus, P., Dugourd, A., Holland, C.H., Ramirez Flores, R.O., and Saez-Rodriguez, J. (2022). decoupleR: ensemble of computational methods to infer biological activities from omics data. Bioinform. Adv. *2*, vbac016.
95. Schubert, M., Klinger, B., Klünemann, M., Sieber, A., Uhlitz, F., Sauer, S., Garnett, M.J., Blüthgen, N., and Saez-Rodriguez, J. (2018). Perturbation-response genes reveal signaling footprints in cancer gene expression. Nat. Commun. *9*, 20.
96. Gu, Z., Eils, R., and Schlesner, M. (2016). Complex heatmaps reveal patterns and correlations in multidimensional genomic data. Bioinformatics *32*, 2847–2849.
97. Gu, Z. (2022). Complex heatmap visualization. Imeta *1*, e43. https://doi.org/10.1002/imt2.43.
98. Andreatta, M., and Carmona, S.J. (2021). UCell: Robust and scalable single-cell gene signature scoring. Comput. Struct. Biotechnol. J. *19*, 3796–3798.
99. Stirling, D.R., Swain-Bowden, M.J., Lucas, A.M., Carpenter, A.E., Cimini, B.A., and Goodman, A. (2021). CellProfiler 4: improvements in speed, utility and usability. BMC Bioinf. *22*, 433.
100. Bankhead, P., Loughrey, M.B., Fernández, J.A., Dombrowski, Y., McArt, D.G., Dunne, P.D., McQuaid, S., Gray, R.T., Murray, L.J., Coleman, H.G., et al. (2017). QuPath: Open source software for digital pathology image analysis. Sci. Rep. *7*, 16878.
101. Ortogero, N., Yang, Z., Vitancol, R., Griswold, M., and Henderson, D. (2023). GeomxTools: NanoString GeoMx Tools. https://doi.org/10.18129/B9.bioc.GeomxTools.
102. Van Der Maaten, L., Courville, A., Fergus, R., and Manning, C. (2014). Accelerating T-SNE Using Tree-Based Algorithms. https://www.jmlr.org/papers/volume15/vandermaaten14a/vandermaaten14a.pdf.
103. Konopka, T. (2023). umap: Uniform Manifold Approximation and Projection.
104. Liberzon, A., Subramanian, A., Pinchback, R., Thorvaldsdóttir, H., Tamayo, P., and Mesirov, J.P. (2011). Molecular signatures database (MSigDB) 3.0. Bioinformatics *27*, 1739–1740.
105. Hänzelmann, S., Castelo, R., and Guinney, J. (2013). GSVA: gene set variation analysis for microarray and RNA-seq data. BMC Bioinf. *14*, 7.
106. Danaher, P., Kim, Y., Nelson, B., Griswold, M., Yang, Z., Piazza, E., and Beechem, J.M. (2022). Advances in mixed cell deconvolution enable quantification of cell types in spatial transcriptomic data. Nat. Commun. *13*, 385.
107. Wang, L., Guo, W., Guo, Z., Yu, J., Tan, J., Simons, D.L., Hu, K., Liu, X., Zhou, Q., Zheng, Y., et al. (2024). PD- L1-expressing tumor-associated macrophages are immunostimulatory and associate with good clinical outcome in human breast cancer. Cell Rep. Med. *5*, 101420.
108. Tietscher, S., Wagner, J., Anzeneder, T., Langwieder, C., Rees, M., Sobottka, B., de Souza, N., and Bodenmiller, B. (2023). A comprehensive single-cell map of T cell exhaustion-associated immune environments in human breast cancer. Nat. Commun. *14*, 98.
109. Sondka, Z., Dhir, N.B., Carvalho-Silva, D., Jupe, S., Madhumita, McLaren, K., Starkey, M., Ward, S., Wilding, J., Ahmed, M., et al.

(2024). COSMIC: a curated database of somatic variants and clinical data for cancer. Nucleic Acids Res. *52*, D1210–D1217.

110. Cameron, D.L., Baber, J., Shale, C., Papenfuss, A.T., Valle-Inclan, J.E., Besselink, N., Cuppen, E., and Priestley, P. (2019). GRIDSS, PURPLE, LINX: Unscrambling the tumor genome via integrated analysis of structural variation and copy number. Preprint at bioRxiv. https://doi.org/10.1101/781013.

111. Cameron, D.L., Baber, J., Shale, C., Valle-Inclan, J.E., Besselink, N., van Hoeck, A., Janssen, R., Cuppen, E., Priestley, P., and Papenfuss, A.T. (2021). GRIDSS2: comprehensive characterisation of somatic structural variation using single breakend variants and structural variant phasing. Genome Biol. *22*, 202.

112. Icay, K., Chen, P., Cervera, A., Rantanen, V., Lehtonen, R., and Hautaniemi, S. (2016). SePIA: RNA and small RNA sequence processing, integration, and analysis. BioData Min. *9*, 20.

113. Cervera, A., Rantanen, V., Ovaska, K., Laakso, M., Nuñez-Fontarnau, J., Alkodsi, A., Casado, J., Facciotto, C., Häkkinen, A., Louhimo, R., et al. (2019). Anduril 2: upgraded large-scale data integration framework. Bioinformatics *35*, 3815–3817.

114. Holmström, S., Hautaniemi, S., and Häkkinen, A. (2022). POIBM: batch correction of heterogeneous RNA- seq datasets through latent sample matching. Bioinformatics *38*, 2474–2480.

115. Zaitsev, A., Chelushkin, M., Dyikanov, D., Cheremushkin, I., Shpak, B., Nomie, K., Zyrin, V., Nuzhdina, E., Lozinsky, Y., Zotova, A., et al. (2022). Precise reconstruction of the TME using bulk RNA-seq and a machine learning algorithm trained on artificial transcriptomes. Cancer Cell *40*, 879–894.e16.

116. Bagaev, A., Kotlov, N., Nomie, K., Svekolkin, V., Gafurov, A., Isaeva, O., Osokin, N., Kozlov, I., Frenkel, F., Gancharova, O., et al. (2021). Conserved pan-cancer microenvironment subtypes predict response to immunotherapy. Cancer Cell *39*, 845–865.e7.

117. Müller-Dott, S., Tsirvouli, E., Vazquez, M., Ramirez Flores, R.O., Badia-I-Mompel, P., Fallegger, R., Türei, D., Lægreid, A., and Saez-Rodriguez, J. (2023). Expanding the coverage of regulons from high-confidence prior knowledge for accurate estimation of transcription factor activities. Nucleic Acids Res. *51*, 10934–10949.

118. Muzellec, B., Teleńczuk, M., VCabeli, V., and Andreux, M. (2023). PyDESeq2: a python package for bulk RNA-seq differential expression analysis. Bioinformatics *39*, btad547. https://doi.org/10.1093/bioinformatics/btad547.

119. Casado, J., Lehtonen, O., Rantanen, V., Kaipio, K., Pasquini, L., Häkkinen, A., Petrucci, E., Hynninen, J., Hietanen, S., Carpén, O., et al. (2021). Agile workflow for interactive analysis of mass cytometry data. Bioinformatics *37*, 1263–1268.

## STAR★METHODS

### KEY RESOURCES TABLE

| REAGENT or RESOURCE | SOURCE | IDENTIFIER |
|---|---|---|
| Antibodies | | |
| FITC Mouse Anti-Human Annexin II | BD Biosciences | Cat#611838; RRID: AB_399318 |
| Alexa Fluor® 555 Anti-alpha smooth muscle Actin antibody [EPR5368] | Abcam | Cat#ab202509; RRID: AB_2868435 |
| CD11c (D3V1E) XP® Rabbit mAb (Alexa Fluor® 555 Conjugate) | Cell Signaling Technologies | Cat#77882; RRID: AB_3331656 |
| Alexa Fluor® 488 Anti-CD163 antibody [EPR14643-36] - C-terminal | Abcam | Cat#ab218293; RRID: AB_2889155 |
| Invitrogen CD20 Monoclonal Antibody (L26), eFluor™ 660, eBioscience™ | Thermo Fisher Scientific | Cat#50-0202-80; RRID: AB_11151691 |
| Human Langerin/CD207 Antibody | R&D Systems | Cat#AF2088; RRID: AB_355143 |
| Alexa Fluor® 647 Anti-CD31 antibody [EPR3094] | Abcam | Cat#ab218582; RRID: AB_2857973 |
| Alexa Fluor® 555 Anti-CD3D antibody [EP4426] | Abcam | Cat#ab208514; RRID: AB_2728789 |
| Human CD4 Alexa Fluor® 488-conjugated Antibody | R&D Systems | Cat#FAB8165G; RRID: AB_2728839 |
| Human CD45 Phycoerythrin MAb (Clone 2D1) | R&D Systems | Cat#FAB1430P; RRID: AB_2237898 |
| Alexa Fluor® 647 anti-human CD45 Antibody | Biolegend | Cat#304018; RRID: AB_389336 |
| CoraLite® Plus 750 Anti-Human CD45 (HI30) | Proteintech | Cat#CL750-65109; RRID: AB_3084850 |
| Alexa Fluor® 488 anti-human CD45RO Antibody | Biolegend | Cat#304212; RRID: AB_528823 |
| Invitrogen CD8a Monoclonal Antibody (AMC908), eFluor™ 660, eBioscience™ | Thermo Fisher Scientific | Cat#50-0008-82; RRID: AB_2574149 |
| Alexa Fluor® 555 Anti-Cytokeratin 7 antibody [EPR17078] | Abcam | Cat#ab209601; RRID: AB_2728790 |
| Alexa Fluor® 647 Anti-Desmin antibody [Y66] - Cytoskeleton Marker | Abcam | Cat#ab195177; RRID: AB_2889196 |
| E-Cadherin (24E10) Rabbit mAb (Alexa Fluor® 488 Conjugate) | Cell Signaling Technologies | Cat#3199S; RRID: AB_10691457 |
| FoxO3a (Ser253) Polyclonal Antibody | Bioss Antibodies | Cat#BS-3140R- AF647; RRID: AB_3451998 |
| Invitrogen FOXP3 Monoclonal Antibody (236A/E7), eFluor™ 570, eBioscience™ | Thermo Fisher Scientific | Cat#41-4777-82; RRID: AB_2573609 |
| Anti-HE4 antibody (Rb-Z) | Abcam | Cat#ab24480; RRID: AB_2216025 |
| Alexa Fluor® 488 Anti-Iba1 antibody [EPR6136(2)] | Abcam | Cat#ab195031; RRID: AB_2889157 |
| Iba1/AIF-1 (E4O4W) XP® Rabbit mAb (Alexa Fluor® 750 Conjugate) | Cell Signaling Technologies | Cat#10420S; RRID: |
| Ki-67 (D3B5) Rabbit mAb (Alexa Fluor® 488 Conjugate) | Cell Signaling Technologies | Cat#11882; RRID: AB_2687824 |
| Alexa Fluor® 488 Anti-Lamin B1 antibody [EPR8985(B)] - Nuclear Envelope Marker | Abcam | Cat#ab194106; RRID: AB_2728786 |
| Alexa Fluor® 647 Anti-HLA A antibody [EP1395Y] | Abcam | Cat#ab199837; RRID: AB_2728798 |
| Alexa Fluor® 647 Anti-HLA-DPB1 antibody [EPR11226] | Abcam | Cat#ab201347; RRID: AB_2861375 |
| Anti-Sodium Potassium ATPase antibody [EP1845Y] - Rat IgG2a (Chimeric) | Abcam | Cat#ab283345; RRID: AB_3451994 |
| Anti-Nectin 2 antibody [EPR6717] | Abcam | Cat#ab135246; RRID: AB_2936435 |
| Invitrogen Pan Cytokeratin Monoclonal Antibody (AE1/AE3), eFluor™ 570, eBioscience™ | Thermo Fisher Scientific | Cat#41-9003-82; RRID: AB_11218704 |
| Alexa Fluor® 555 Anti-PAX8 antibody [EPR18715] | Abcam | Cat#ab217733; RRID: AB_3451995 |
| Alexa Fluor® 647 Anti-PD1 antibody [EPR4877(2)] | Abcam | Cat#ab201825; RRID: AB_2728811 |
| Phospho-Stat1 (Tyr701) (58D6) Rabbit mAb (Alexa Fluor® 555 Conjugate) | Cell Signaling Technologies | Cat#8183S; RRID: AB_10860600 |
| SNAT1 Mouse anti-Human | MilliporeSigma | Cat#MABN502; RRID: AB_2716561 |
| YAP/TAZ (D24E4) Rabbit mAb | Cell Signaling Technologies | Cat#8418; RRID: AB_10950494 |

(*Continued on next page*)

***Continued***

| REAGENT or RESOURCE | SOURCE | IDENTIFIER |
|---|---|---|
| IHC-plus™ Monoclonal Mouse anti-Human TIGIT Antibody | LifeSpan Biosciences | Cat#LS-B16022; RRID: AB_3451997 |
| TIM-3 (D5D5R™) XP® Rabbit mAb (Alexa Fluor® 488 Conjugate) | Cell Signaling Technologies | Cat#54669S; RRID: AB_2799468 |
| Vimentin (D21H3) XP® Rabbit mAb (Alexa Fluor® 555 Conjugate) | Cell Signaling Technologies | Cat#9855S; RRID: AB_10859896 |
| Vimentin (D21H3) XP® Rabbit mAb (Alexa Fluor® 750 Conjugate) | Cell Signaling Technologies | Cat#69227S; RRID: AB_3331655 |
| Alexa Fluor® 647 anti-H2A.X Phospho (Ser139) Antibody | Biolegend | Cat#613407; RRID: AB_2114994 |
| Invitrogen Goat anti-Mouse IgG (H+L) Highly Cross-Adsorbed Secondary Antibody, Alexa Fluor™ Plus 555 | Thermo Fisher Scientific | Cat#A32727; RRID: AB_2633276 |
| Invitrogen Goat anti-Mouse IgG (H+L) Cross-Adsorbed Secondary Antibody, Alexa Fluor™ 647 | Thermo Fisher Scientific | Cat#A21235; RRID: AB_2535804 |
| Invitrogen Goat anti-Rabbit IgG (H+L) Highly Cross-Adsorbed Secondary Antibody, Alexa Fluor™ 488 | Thermo Fisher Scientific | Cat#A11034; RRID: AB_2576217 |
| Goat anti-Rat IgG (H+L) Cross-Adsorbed Secondary Antibody, Alexa Fluor™ 555 | Thermo Fisher Scientific | Cat#A21434; RRID: AB_2535855 |
| Cytokeratin, pan Antibody (AE-1/AE-3) - Azide and BSA Free | Novus | Cat#NBP2-33200; RRID: AB_3284598 |
| 0BCD45 Antibody (2B11 + PD7/26) - Azide and BSA Free | Novus | Cat#NBP2-34528; RRID: AB_2864384 |
| Mouse anti-human CD56 FITC-conjugated | Immunotools | Cat#21270563; RRID: AB_3251502 |
| Mouse anti-human CD14 PE-conjugated | Immunotools | Cat#21620144; RRID: AB_3251503 |
| BD Horizon™ PE-CF594 Mouse anti-Human CD4 | BD Biosciences | Cat#562281; RRID: AB_11154597 |
| BD Pharmingen™ PerCP-Cy™5.5 Mouse Anti-Human HLA-DR | BD Biosciences | Cat#552764; RRID: AB_394453 |
| BD Pharmingen™ PE-Cy™7 Mouse anti-Ki-67 | BD Biosciences | Cat#561283; RRID: AB_10716060 |
| Granzyme B Monoclonal Antibody (GB11), APC | Invitrogen | Cat#GRB05; RRID: AB_2536539 |
| BD Pharmingen™ Alexa Fluor® 700 Mouse Anti-Human IFN-Û | BD Biosciences | Cat#557995; RRID: AB_396977 |
| APC/Fire™ 750 anti-human CD326 (EpCAM) Antibody | Biolegend | Cat#324233; RRID: AB_2629702 |
| BD Horizon™ BV421 Mouse Anti-Human CD45 | BD Biosciences | Cat#563880; RRID: AB_2744402 |
| BD Horizon™ BV605 Mouse Anti-Human CD8 | BD Biosciences | Cat#564116; RRID: AB_2869551 |
| BD Horizon™ BV711 Mouse Anti-Human CD11c | BD Biosciences | Cat#563130; RRID: AB_2738019 |
| BD Horizon™ BV786 Mouse Anti-Human CD3 | BD Biosciences | Cat#563800; RRID: AB_2744384 |
| Pembrolizumab (anti-PD-1) | Selleckchem | Cat#A2005 |
| Tiragolumab (anti-TIGIT) | Selleckchem | Cat#A2028 |
| Biological samples | | |
| HGSC tumor/ascites samples | DECIDER study (NCT04846933), Turku University Hospital<br>Oncosys-OVA study (NCT06117384), Helsinki University Hospital | S001-S047<br>C063 C063 C033 C033 C686 C686<br>C879 C538 C799 C917 C790 C423<br>C129 C129 C535 C535 C893 C538<br>C799 C917 C790 C972 C129 C985<br>C433 C331 C369 C344 C758 C426<br>C137 C946 C078 C791 C663 C804<br>iPDCs: C659, C973, C817, C944, C661, C181, C696, C732, C041, C215, C024 |
| Chemicals, peptides, and recombinant proteins | | |
| Advanced DMEM/F12 | Thermo Fisher Scientific | Cat#12634-010 |
| Primocin | Invivogen | Cat#ANTPM1 |
| MEM Non-Essential Amino Acids Solution (100X) | Thermo Fisher Scientific | Cat#11140035 |
| Sodium Pyruvate (100 mM) | Thermo Fisher Scientific | Cat#11360039 |
| GlutaMAX™ Supplement | Thermo Fisher Scientific | Cat#35050061 |
| HEPES solution | Sigma-Aldrich | Cat#H0887-100ML |
| N-Acetyl-L-cysteine | Sigma-Aldrich | Cat# A9165-100G |
| Nicotinamide | Sigma-Aldrich | Cat#N0636-500G |

(*Continued on next page*)

*Continued*

| REAGENT or RESOURCE | SOURCE | IDENTIFIER |
|---|---|---|
| B-27™ Supplement (50X), serum free | Thermo Fisher Scientific | Cat#17504044 |
| Recombinant Human FGF-10 | Peprotech | Cat#100-26 |
| Animal-Free Recombinant Human FGF-basic (154 a.a.) | Peprotech | Cat#AF-100-18B |
| A-83-01 | Sigma-Aldrich | Cat# SML0788-5MG |
| ù-Estradiol | Sigma-Aldrich | Cat# E2758-1G |
| 5HFRPELQDQW +XPDQ +HUHJXOLQù-1 | Peprotech | Cat#100-03 |
| Animal-Free Recombinant Human EGF | Peprotech | Cat#AF-100-15 |
| Hydrocortisone | Sigma-Aldrich | Cat#H0888-1G |
| Y-27632 dihydrochloride | AbMoleBiosciences | Cat#M1817 |
| Recombinant Human IL-2 | Peprotech | Cat#200-02 |
| Recombinant Human IL-15 | Peprotech | Cat#200-15 |
| Recombinant Human IL-7 | Peprotech | Cat#200-07 |
| DMEM/F-12 | Thermo Fisher Scientific | Cat#11320033 |
| Penicillin-Streptomycin (10,000 U/mL) | Thermo Fisher Scientific | Cat#15140122 |
| Dispase® II | Sigma-Aldrich | Cat#D4693 |
| RQ1 RNase-Free DNase | Promega | Cat#M6101 |
| Red Blood Cell Lysis Buffer | Merck | Cat#11814389001 |
| Hoechst 33342, trihydrochloride trihydrate | Thermo Fisher Scientific | Cat#H3570 |
| Invitrogen™ LIVE/DEAD™ Fixable Aqua Dead Cell Stain Kit, for 405 nm excitation | Thermo Fisher Scientific | Cat#L34965 |
| Critical commercial assays | | |
| Chromium™ Single Cell 3’ Library & Gel Bead Kit v2 | 10x Genomics | PN-120237 |
| Chromium™ Single Cell 3’ Chip Kit v2 | 10x Genomics | PN-120236 |
| Chromium™ i7 Multiplex Kit | 10x Genomics | PN-120262 |
| &KURPLXP 6LQJOH &HOO 30)* ↄ, /LEUDU\ & *HO %HDG .LW Y3 | 10x Genomics | PN-1000075 |
| Chromium Single Cell B Chip Kit | 10x Genomics | PN-1000073 |
| &KURPLXP 1H[W *(0 6LQJOH &HOO 30)* ↄ, /LEUDU\ & *HO Bead Kit v3.1 | 10x Genomics | PN-1000121 |
| Chromium Next GEM Chip G Single Cell Kit | 10x Genomics | PN-1000120 |
| Dual Index Kit TT Set A | 10x Genomics | PN-1000215 |
| GeoMx Human Whole Transcriptome Atlas Human RNA for Illumina Systems | nanoString | GMX-RNA-NGS- HuWTA-4 |
| Deposited data | | |
| Processed scRNA-seq data | GEO | GSE266577<br>This GEO series also includes preprocessed count data originally published in https://doi.org/10.1126/sciadv.abm1831, https://doi.org/10.1093/bioinformatics/btab178, https://doi.org/10.1371/journal.pcbi.1009290 and https://doi.org/10.1016/j.devcel.2023.04.012, as listed in Table S7. |
| Processed t-CycIF data | Synapse | https://doi.org/10.7303/syn53283672 |
| Preprocessed GeoMx data and metadata | Synapse | https://doi.org/10.7303/syn53283672 |
| Raw Flow Cytometry data from iPDC drug testing experiments | Synapse | https://doi.org/10.7303/syn53283672 |
| Raw WGS data from the DECIDER cohort | EGA | EGAS00001006775<br>This data have been originally published in https://doi.org/10.1016/j.ccell.2023.04.017 |

(*Continued on next page*)

*Continued*

| REAGENT or RESOURCE | SOURCE | IDENTIFIER |
|---|---|---|
| Raw bulk RNAseq data from the DECIDER cohort | EGA | EGAS00001004714<br>This data have been originally published in https://doi.org/10.1016/j.ccell.2023.04.017 |
| Software and algorithms | | |
| Cell Ranger v.6.0.1 | 10x Genomics | https://www.10xgenomics.com/support/software/cell-ranger/latest |
| R package MultiNicheNetR v.1.0.0 | Browaeys et al.[43] | https://github.com/saeyslab/multinichenetr |
| R package miloR v.1.5.0 | Dann et al.[42] | https://github.com/MarioniLab/miloR |
| R package Seurat v.4.3.0 | Hao et al.[88], Stuart et al.[89] | https://satijalab.org/seurat/articles/install_v5 |
| R package ProjectTILs v.3.3.1 | Andreatta et al.[98] | https://github.com/carmonalab/ProjecTILs |
| R package ComplexHeatmap v.2.20.0 | Gu[97], Gu et al.[96] | https://bioconductor.org/packages/release/bioc/html/ComplexHeatmap.html |
| R package speckle v.0.0.3 | Phipson et al.[90] | https://github.com/phipsonlab/speckle |
| R package tidyverse v.2.0.0 | CRAN | https://tidyverse.tidyverse.org/ |
| R package progeny v.1.12.0 | Schubert et al.[95] | https://bioconductor.org/packages/release/bioc/html/progeny.html |
| Python package celltypist v.0.1.9 | Domínguez Conde et al.[35] | https://pypi.org/project/celltypist/ |
| FlowJo™ v10.9.0 Software | BD Life Sciences | https://www.flowjo.com/ |
| Cyto | Casado et al.[119] | https://bitbucket.org/anduril-dev/cyto/wiki/browse/ |
| Tribus | Kang et al.[34] | https://github.com/farkkilab/tribus |
| CellProfiler | Stirling et al.[99] | https://cellprofiler.org/ |
| QuPath | Bankhead et al.[100] | https://qupath.github.io/<br>https://github.com/qupath/qupath |
| R package GeomxTools | Ortogero et al.[101] | https://www.bioconductor.org/packages/release/bioc/html/GeomxTools.html |
| R package BayesPrism | Chu et al.[55] | https://github.com/Danko-Lab/BayesPrism |
| R package SpatialDecon | Danaher et al.[106] | https://bioconductor.org/packages/release/bioc/html/SpatialDecon.html |
| R package Rtsne | Van Der Maaten et al.[102] | https://github.com/jkrijthe/Rtsne |
| R package umap | Konopka[103] | https://github.com/tkonopka/umap |
| R package GSVA | Hänzelmann et al.[105] | https://bioconductor.org/packages/release/bioc/html/GSVA.html |
| R package ovaHRDscar | Perez-Villatoro et al.[77] | https://github.com/farkkilab/ovaHRDscar |
| PURPLE algorithm | Cameron et al.[110] | https://github.com/hartwigmedical/hmftools/tree/master |
| GRIDSS2 algorithm | Cameron et al.[111] | https://github.com/PapenfussLab/gridss |
| SePIA pipeline | Icay et al.[112] | https://anduril.org/sepia/ |
| POIBM method | Holmström et al.[114] | https://doi.org/10.5281/zenodo.6122436 |
| R package PRISM | Häkkinen et al.[51] | https://bitbucket.org/anthakki/prism/src/master/ |
| Kassandra deconvolution algorithm | Zaitsev et al.[115] | https://github.com/BostonGene/Kassandra |
| R package decoupleR | Badia-i-Mompel et al.[94] | https://github.com/saezlab/decoupleR |
| Python package DESeq2 | Muzellec et al.[118] | https://bioconductor.org/packages/release/bioc/html/DESeq2.html |
| BaSiC tool and ASHLAR algorithm | Muhlich et al.[80] | https://github.com/labsyspharm/ashlar |
| UNET | Ronneberger et al.[81] | |
| R Package Giotto | Dries et al.[82] | https://rubd.github.io/Giotto_site/ |
| R Package spatstat | Baddeley et al.[83] | https://spatstat.org/ |
| Python package scimap | Nirmal et al.[29] | https://scimap.xyz/ |

(*Continued on next page*)

*Continued*

| REAGENT or RESOURCE | SOURCE | IDENTIFIER |
|---|---|---|
| R package SYNCSA | Debastiani and Pillar[84] | https://github.com/vanderleidebastiani/SYNCSA |
| Python package Squidpy | Palla et al.[85] | https://squidpy.readthedocs.io/en/stable/ |
| STARDIST | Schmidt et al.[87] | https://github.com/stardist/stardist |
| Custom scripts related to this paper | This paper | https://doi.org/10.5281/zenodo.13849272 |

## EXPERIMENTAL MODEL AND STUDY PARTICIPANT DETAILS

### Cohort description

Tumor samples and clinical data were collected in two independent prospective clinical trials; DECIDER NCT04846933, and Oncosys-OVA NCT06117384. The patients' clinical details are summarized in Tables 1 and S1. For triaging the patients to undergo NACT, ESMO-ESGO 2019 guidelines[13] were utilized. Patients with no tumor cells identified by pathologist at IDS samples were excluded from the paired scRNA-seq analyses. Platinum-free interval (PFI) was calculated from the last day of dosage of the platinum chemotherapy to disease relapse. Patients with PFI >12 months were considered platinum sensitive and categorized as patients with long PFI.[73] Samples for WGS, bulk RNA-seq, scRNA-seq and t-CyCIF were collected from the DECIDER study of patients with HGSC treated at the Turku University Hospital, Finland. Tumor specimens (scRNA-seq: n=51, t-CyCIF n=22, bulk RNA-seq n=60, WGS n=60) were collected from HGSC patients (n=44) at the time of laparoscopy or primary debulking surgery (PDS) (chemo-naive) and interval debulking surgery (IDS) (STAR Methods). In addition to newly produced scRNA-seq data from 25 tumors, the scRNA-seq cohort contains data from three clinical specimens originally published in,[51] 21 specimens originally published in,[21] and two specimens originally published in.[74] Genomic HRD annotations were previously published in,[75–77] and bulk RNAseq in.[78] The DECIDER study was approved by the Wellbeing Services County of Southwest Finland (VARHA/28314/13.02.02/2023). Tumor samples for t-CyCIF, GeoMx, bulk RNA-seq and WES (n=16), and the IDS tumor samples for t-CyCIF staining (n=20) were collected from patients participating in the prospective ONCOCYS-OVA study approved by the Ethics Committee of the Helsinki University Hospital (HUS334/2021).

Samples for iPDCs generation and drug-testing experiments were collected from the Oncosys-OVA study of patients with HGSC treated at the Helsinki University Hospital, Finland. Tumor specimens were collected from HGSC at the time of primary debulking surgery (n=5) and IDS (n=6).

In accordance with the ethical standards from the 1975 Declaration of Helsinki, every patient from DECIDER and ONCOSYS-Ova trials provided an informed written consent to the collection, storage, and analysis of the samples and subsequent data.

## METHOD DETAILS

### Highplex t-CyCIF imaging and image processing

The samples were stained consecutively with the validated antibodies (Table S5 related to STAR Methods, experiment 1) followed by scanning with the RareCyte CyteFinder scanner with the t- CyCIF protocol.[79] The image files were corrected, stitched, and registered using the BaSiC tool and ASHLAR algorithm.[80] The raw ome-tiff images were segmented into cells based on probability maps created by UNET[81] with a modified version of the S3Segmenter algorithm (https://github.com/HMS-IDAC/S3segmenter). Cytoplasm segmentation masks were created by expanding the nuclei region with a 2-pixel ring dilation. Each cell's mean fluorescence intensity was computed by Python's scikit- image library using in-house scripts (https://github.com/farkkilab/image_processing/blob/main/pipeline/quantification_workflow.py). In total over the 22 whole slide images 8,912,899 cells were identified, from which first 1,448,531 cells were removed by cycifsuite's detect_lost_cells function (https://github.com/yunguan-wang/cycif_analysis_suite/tree/MCF10A/cycifsuite) due to tissue movement or detachment. Further quality control was carried out in the Napari image viewer, and artifacts (hairs, folds, bubbles) were removed by manual area selection, affecting 43,470 cells.

### t-CyCIF cell phenotyping

Log transformation was applied to the quantified single-cell signals. TRIBUS[34] recently developed in our lab was first used to assign cells semi-automatically and iteratively into cell types using SOM- based clustering with single-cell feature quantification table and cell phenotype marker positivity and negativity as inputs. The markers used for cell type characterization are shown in Table S6. First, tumor cells were separated from non-tumor cells, after which non-tumor cells were categorized into stromal, myeloid, and lymphoid cells, and these further into subtypes. The tumor cells were also separated to metaclusters using the expressions of CK7, E-cadherin, Ki67 and vimentin, and stromal cells were subcategorized into metaclusters using the expressions of SMA, Vimentin, CD31, CK7 and Desmin. Cells that were not assigned to any of the mentioned categories were labeled as "Other" (mean 14% of the cells per sample), these mostly resided at the stromal areas. Quality control for the cell type calls was performed using the *pl.image_viewer* function in Scimap-toolkit[29] in python by overlaying the cell type calls on top of the images. Cells that had been mislabeled, mostly B cells as "other" cells, were reclassified using the *pl.gate_finder(), pl.addROI_image()* and *hl.classify()* functions separately for each image for selected areas. The scimap functions *pl.gate_finder()* and *pp.rescale()* were used to rescale the functional markers per image (Ki67, Annexin A2, TIM3, pSTAT1, TAZ, MHC-I, MHC-II, CD45RO, SNAT1).

### t-CycIF spatial analysis

Cell-cell interactions with CD8$^+$ and CD4$^+$ T cells and their relationships to functional marker expression by tumor cells and myeloid cells were computed using the Giotto package in R.[82] The *FindInteractionChangedFeats* function with Delaunay network was used separately for each image to find the fold changes for markers which changed based on the spatial interaction with another celltype. Delaunay networks for the analysis of myelonets were calculated using the spatstat package[83] in R, with the maximum length between edges 45 pixels.

Recurrent cellular neighborhoods (RCNs) were computed using the Scimap package[29] in python, by first calculating the fractions of neighboring cell types for each centering cell using *tl.spatial_count* with a r=100px, and the resulting neighborhood matrix was then clustered using *tl.spatial_cluster* using kmeans clustering with k=18. 100 pixel radius was chosen to find large scale cellular structures from the single-cell spatial data, the radius encompasses around 3-4 cells in length. The identity of each cluster was defined by the proportions of cell types composing it, and by overlaying these on top of the images using the *pl.image_viewer* function in scimap. The Rao's quadratic entropy per RCN was computed using the *rao.diversity* function in the SYNCSA R-package,[84] with cell type proportions and functional marker expressions as inputs. Furthermore, the cell-cell interaction and avoidance patterns compared to a random background were computed using the *tl.spatial_interaction* function from the scimap-package with a radius of 45 pixels.

Centrality scores were calculated using the Squidpy[85] package in python separately for each image for each cell type with the *gr.centrality_scores* function.

### Low-plex t-CycIF staining and image processing

The samples were stained with twelve/seven/eleven antibodies (Table S5, experiments 2, 3 and 4) following the t-CycIF protocol.[79] Images were obtained within the Pathology Department at the University of Helsinki, employing a high-throughput scanner equipped with an ECLIPSE Ni-E body, an ORCA-Flash4.0 LT PLUS camera by Hamamatsu, and a Märzhäuser Slide Express slide loader. Tile stitching and registration across different cycles were performed similarly as for highplex t-CycIF images. Nuclei segmentation was carried out by STARDIST.[86,87] Single-cell information was extracted similarly as for highplex t-CycIF images for 10,082,019 cells, 8,829,233 cells and 8,305,429 cells for experiments 2, 3 and 4 respectively.

### Low-plex t-CycIF cell type calling

Cell type calling for low-plex t-CycIF was performed using the *pl.gate_finder*, *pp.rescale, tl.phenotype* and *hl.classify* functions for each marker (Table S5) for each image in scimap-toolkit[29] in Python. The cell type calls were confirmed by overlaying them on top of the images using the *pl.image_viewer* function in scimap. Recurrent cellular neighborhoods were computed using the *tl.spatial_count* with r=100px and *tl.spatial_cluster* functions, with k-means clustering using k=10 and k=8 for experiments 2 and 3 (Table S5).

### Sample preparation for scRNA-seq

Tumor specimens were incubated overnight in a mixture of collagenase and hyaluronidase (Department of Pathology, University of Turku) to obtain single-cell suspensions. Chromium Single- &HOO 3ǫ 5HDJHQW .LW Y.2.0 DQG Y.3.0 (10[ *HQRPLFV) ZHUH XVHG WR SUHSDUH scRNA-seq libraries.

Libraries were sequenced on Illumina HiSeq 4000 (Jussi Taipale Lab, Karolinska Institute, Sweden), HiSeq 2500, and NovaSeq 6000 instruments (Sequencing Unit of the Institute for Molecular Medicine Finland, Finland).

### Preprocessing scRNA-seq data

The published data (Table S7) were jointly processed with the new data produced for this study as follows. The fastq files were processed with the Cell Ranger v.6.0.1 pipeline (10x Genomics) for demultiplexing, alignment, barcode processing, and unique molecular identifier (UMI) quantification. Gene annotation was done using GENCODE v25 and GRCh38.d1.vd1 was used as reference genome. The count matrices were loaded into Seurat (v3.2.2)[88,89] and dimensionality reduction and initial clustering using k-means were performed using the UMAP algorithm. Based on marker expression, cells were assigned to three major cell types: epithelial tumor cells (*WFDC2*, *PAX8*, *MUC16*), stromal cells (*COL1A2*, *FGFR1*, *DCN*), and immune cells (*CD79A*, *FCER1G*, *PTPRC*). miQC[74] was used separately per each cell type to filter out cells with high proportion of mitochondrial reads or low number of genes without assigning a hard threshold. The cells expressing a combination of *DCN*, *PAX8* or *PTPRC* were also filtered to exclude possible doublets. After initial filtering, dimensionality reduction, clustering and cell-type assignment were performed again. Moreover, to ensure high-quality cells for downstream analysis, stromal cells with a number of UMI (in log scale) <11, immune cells with < 10.5 and tumor cells with <12 were removed through further filtering.

### Cell type annotation in scRNA-seq data

The celltypist[35] Python package (v.0.1.9) was used for automated annotation of cell types. The predicted cell type labels were acquired by running the function *celltypist.annotate*(model = 'Immune_All_Low.pkl', majority_voting = True). This model contains curated immune sub- populations combined from 20 tissues of 18 studies as described in[35] to reliably infer the cell type labels from an established and broad cross-tissue immune cell atlas.

### Identifying macrophage states in scRNA-seq data

To identify similar macrophage states in the scRNA-seq data, we re-annotated the macrophages based on *CD163* and *ITGAX* expression. We used Seurat::FindMarkers(test.use = ''wilcox'', logfc.threshold = 0.25, min.pct = 0.1) function to identify genes differentially expressed between *CD163*$^+$ and *ITGAX*$^+$ macrophages. To calculate *CD163* and *ITGAX* gene module scores, we divided the list of differentially expressed genes into two groups based on logFC (logFC >0, CD163 gene module; logFC < 0, ITGAX gene module). Then, we used UCell::AddModuleScore() function to calculate the gene module scores.

To identify whether macrophage polarization was associated with clinical response, we calculated the mean *CD163* and *ITGAX* gene module scores for each patient and compared them between patients with short PFI and those with long PFI.

### Identifying CD8$^+$ T cell states in scRNA-seq data

To identify the CD8$^+$ T cell states in the scRNA-seq data, we used the ProjectTIL R package.[48] The ProjecTILs.classifier() function was run using the reference atlas of CD8$^+$ tumor-infiltrating T cells (version 2; published by Andreatta et al.[48]) as the reference data set, without pre-filtering any cells.

### Differential cell abundance analysis in scRNA-seq data

We used the speckle R package[90] to calculate the changes in cell proportions after NACT. The cell proportions were logit transformed, and the *propeller* function was run to perform linear modeling to calculate the changes in cell proportions between IDS and chemo-naive samples in a pairwise fashion.

As the secondary approach, we used a robust strategy for differential abundance testing for scRNA- seq data.[42,91] The Milo framework models cell states as neighborhoods on a nearest neighbor graph and uses a negative binomial generalized linear model for hypothesis testing to identify differentially abundant neighborhoods between conditions of interest between (chemo-naive vs IDS samples).

We created a Milo object from the Seurat object, and built a k-nearest neighbors (KNN) graph with the function *buildGraph*(k = 200, d = 10), and created neighborhoods with the function *makeNhoods*(prop = 0.05, k = 200, d = 10, refined = TRUE). We counted the cells in the neighborhoods with the *countCells* function and calculated the distances between the neighborhoods with the *calcNhoodDistance* function. We created a design matrix using the metadata and ran the *testNhoods* function with the design (∼ 0 + class) to find the differentially abundant T cell state neighborhoods between chemo-naive and IDS samples.

To further analyze gene expression in the Milo identified IDS enriched macrophage neighborhoods, we performed differential expression analysis (DEA) between pure macrophage neighborhoods that showed statistically significant enrichment in the IDS samples (cell_type == "Macrophages" & cell_type_fraction == 1 & logFC > 0 & SpatialFDR < 0.05) and those that did not show statistically significant changes (cell_type == "Macrophages" & cell_type_fraction == 1 & SpatialFDR >= 0.05). Seurat's *FindMarkers()* function was used to identify differentially expressed genes above the specified threshold (logfc.threshold = 0.25) in at least 10% of the cells (min.pct = 0.10), using the Wilcoxon test (test.use = ''wilcox'').

The clusterProfiler R package[92,93] was used to perform overrepresentation analysis (ORA). The *enrichGO()* function was used to identify enriched gene ontology (GO) biological processes (BP) related to genes with higher expression in macrophages enriched in the IDS samples (pAdjustMethod = "BH", pvalueCutoff = 0.01, qvalueCutoff = 0.05), and a dot plot was used to visualize the top 10 terms.

### Ligand-receptor interaction analysis

The MultiNicheNet framework[43] was used to infer the changes in cell-cell interactions after NACT. We utilized the scRNA-seq data from 22 paired chemo-naive and IDS samples from the same patients, and subsetted the Seurat object to retain cell types of interest (''Macrophages'', ''Epithelial cells'', ''Tem/Trm cytotoxic T cells'') in paired chemo-naive and IDS samples from matched patients.

The *multi_nichenet_analysis* function was run with the following parameters: sample_id = "sample'', group_id = "class", celltype_id = "cell_type", covariates = "patient", batches = NA, min_cells = 10, contrasts_oi = c("'interval-primary','primary-interval'"), logFC_threshold = 0.75, p_val_threshold = 0.05, fraction_cutoff = 0.10, p_val_adj = TRUE, empirical_p_value = FALSE, top_n_target = 250. We used the *get_top_n_lr_pairs* function to filter the top 50 ligand-receptor interactions across all contrasts and used the *make_circos_group_comparison* function to create the circos plots to visualize the predicted interactions.

For ligand-receptor interactions specific to macrophages and CD8$^+$ T cells, we selected the top 50 predicted interactions, ranked them based on scaled ligand activity in receiver cells (i.e., enrichment of the predicted target genes of the ligand in CD8$^+$ T cells), and used the *make_sample_lr_prod_activity_plots* function to visualize the top30 ligand-receptor pseudobulk product expression across samples and ligand activity in the same plot.

### Pathway activity inference in scRNA-seq data

We used the decoupleR R package[94] to infer the activities of 14 signaling pathways in cell types present in the chemo-naive and IDS samples. The *get_progeny* function was used to access the gene weights for the top 500 genes stored in the PROGENy R package[95] and the *run_ulm* function was used for univariate linear modeling on the normalized count matrix extracted from the Seurat object. The ComplexHeatmap R package[96,97] was used to visualize the scaled pathway activity scores across cell types. The same approach was used to compare pathway activities in macrophages.

### Linear mixed models

Individual multiple linear regression models were created for each of the six genes of interest with base lm() function from R and using the immune compartment from bulk RNAseq deconvoluted with PRISM.[51] Each model tried to predict the average change on expression pre and post-treatment of the relevant genes detected in the ligand-receptor interaction analysis using genomic and clinical features, namely PFI, proportion of shared mutations in chemo-naive compared to post-NACT and vice versa, ploidy, tumor purity and HRD status. F statistic was calculated to assess the overall fitness of the model coefficients and adjusted p-values for each independent variable from the models were jointly plotted as a histogram.

### Quantification of T cell exhaustion in scRNA-seq data

We used the UCell algorithm[98] by running the AddModuleScore_UCell function with default parameters to calculate the module score for a gene set linked to T cell exhaustion.[62] The base::mean() function was used to calculate the average module scores for each sample. Paired samples Wilcoxon test was used to compare average T cell exhaustion scores between paired chemo-naive and IDS samples. The complete list of genes is shown in Table S8.

### GeoMx

The GeoMx spatial transcriptomics procedure was conducted at the Single Cell Analytics unit within the Institute for Molecular Medicine Finland (FIMM), adhering to the prescribed GeoMx guidelines for slide staining and scanning. The human Solid Tumor TME morphology marker kit was employed for this purpose. The tissue slide chosen to perform GeoMx sequencing was adjacent to the one on which lowplex t-CyCIF have been performed, to enable guided ROI selection.

### GeoMx ROI selection with lowplex t-CyCIF crop overlay

Lowplex t-CyCIF stainings were employed to guide the selection of regions of interest (ROIs, n=160) in the GeoMx experiment. The chosen regions contained tumor-stroma interface features, indicated by the presence of PanCK$^+$ and Vimentin$^+$ cells, and a variety of CD8 (CD8$^+$ T cells) and IBA1 (macrophages) staining markers for optimal ROI identification within the t-CyCIF crop (CD8$^+$IBA1$^+$, CD8$^+$IBA1$^-$, CD8$^-$IBA1$^+$, CD8$^-$IBA1$^-$). The ROIs were selected based on the relative abundance of CD8$^+$ and IBA1$^+$ cells observed within a given slide. The chosen t-CycIF crop was imported into the GeoMx software and manually superimposed onto the GeoMx scan using landmarks present in both images. Consistency in choosing similar types of areas, avoiding tissue folds, necrotic regions, or adipose tissue, while maintaining similarities in ROI size, tumor-stroma ratio and cell count across all samples was aimed. An external segmentation pipeline generated in CellProfiler[99] was employed to establish distinct areas of Illumination (AOIs, n=320) separately for the tumor and stromal compartments.

### GeoMx and t-CyCIF data pairing

Whole slide image alignment was achieved in QuPath[100] through the Warpy plugin, which performs affine registration, incorporating the moving image to the coordinate system of the base image. The resulting files were exported as pyramidal ome.tiff files to be analyzed in other platforms.

### GeoMx data quality control and preprocessing

DCC files obtained from the sequence provider were handled with the usage of GeomxTools R package,[101] provided by Nanostring. Segment (AOI) and probe level QC were performed as described in the package vignette. Overall, four AOIs were removed due to insufficient quality, and remaining 316 were further processed. Only one probe was removed from the dataset due to insufficient quality. Later, counts for the probes targeting the same gene were aggregated. Additional QC was performed, based on LOQ (limit of quantification), as described in the GeomxTools vignette. Since we expected a high level of variance in our dataset, Gene Detection Rate parameter was set up to 0.01 (gene was removed if expression > LOQ in more than 1% of AOIs). Almost 2000 genes and none of the AOIs were removed during this procedure, leaving a total number of 16,727 genes detected in the whole dataset with sufficient quality.

Next, data was normalized using Q3 quartile normalization method from GeomxTools package and dimensionality reduction was performed using t-distributed stochastic neighbor embedding (t-SNE) and UMAP methods using Rtsne[102] and umap[103] R packages.

### GeoMx pathway activity analysis and correlation analysis on the full transcriptomics signal

We selected 19 pathways from the MSigDB database,[104] from Hallmark and Canonical Pathways collections, to compare their activities within different types of AOI and clinical features of the patients. Selected pathways were connected with the processes such as regulation of T cells, macrophages and cancer cell biology, and immune response. T cell exhaustion related gene set was retrieved from Zheng et al.[62] The full list of selected pathways can be found in Table S3. Q3 normalized gene expression matrix was used for pathway analysis. Selected pathway activities were inferred using the GSVA method with Poisson kernel from the GSVA[105] R package.

Statistical significance of the differences between pathways activities between IDS and chemo-naive samples, per each AOI type, was calculated using a two-sided Wilcoxon rank-sum test.

We used Spearman correlation for analyzing the correlations between pathways in CD8$^+$IBA1$^+$ ROIs. We grouped all pathways into groups resembling important biological signaling axis: T cell exhaustion, IL2-JAK-STAT, TNFα-NFκB, IFNγ, M1 and M2 macrophages, MHC presentation and epithelial to mesenchymal transition (EMT) (Table S4). Next, we calculated correlation coefficients and p-values for all pairs of pathways and counted a number of significant correlations (p-value <= 0.05, spearman correlation coefficient > 0.6). We analyzed only positive correlations, since no significant negative correlations were found within our data. At the end we compared the number of significant correlations between groups of pathways, separately for tumor and stromal compartments and chemo-naive and IDS samples.

### GeoMx signal deconvolution

Since GeoMx data for each AOI contains a mixture of signals derived from each cell type within TME, we performed deconvolution of the signal to obtain the cell-type specific transcriptional profiles. To do that, we utilized 2 methods: 1) BayesPrism[55] - designed for deconvolution of bulk RNAseq data, but validated on various spatial transcriptomics data, which apart from the fraction of cell types is able to compute the cell-type specific transcriptomics profiles 2) SpatialDecon[106] - method designed specifically for GeoMx spatial transcriptomics data, returning fractions of given cell types. Since both methods are based on reference scRNA data, we utilized our annotated ovarian cancer scRNA-seq dataset, described above. We downsampled the full dataset in a patient-specific manner, generating the final dataset containing 24560 cells and 33458 genes. Due to the limitations of both algorithms to correctly predict fractions of fine-grained immune cell types, we decided to cluster similar cell types into more general groups. Finally, as a reference for deconvolution algorithms, we used scRNA-seq profiles of: 9168 T cells (Regulatory T cells, Tcm/Naive helper T cells, Tem/Trm cytotoxic T cells, Type 17 helper T cells), 5240 tumor cells, 4364 macrophages (Classical monocytes, macrophages), 2335 fibroblasts, 1515 B cells (Memory B cells, Naive B cells, Plasma cells), 1007 NK cells ($CD16^-$ NK cells, $CD16^+$ NK cells, NK cells), 403 Dendritic cells (DC1, DC2, Migratory DCs, pDC), 287 mast cells, 90 endothelial cells and 151 ‘other’ cells (ILC, Late erythroid cells).

For BayesPrism method we performed deconvolution according to their vignette (see key resources table), filtering out low complexity genes from our downsampled scRNA-seq dataset, using above mentioned cell groups as ‘cell types’ and ‘cell states’ annotation (for cell states, tumor cells from each patient were annotated separately). For SpatialDecon we followed their vignette (see key resources table), using a custom profile matrix prepared using our downsampled scRNA-seq dataset. For both methods, we used raw scRNA-seq counts and Q3 normalized GeoMx data.

Finally, to validate the results, we compared the cell type fractions obtained from both methods (Figures S5F–S5H). We found sufficient concordance for the fractions of immune cell types, although in some cases the methods differed noticeably in the estimated number of tumor cells. Demonstrating the relevance of our results, we used cell-type specific transcriptomics profiles of macrophages and T cells for the subsequent analysis. Using these results we re-labeled ROIs using the following procedure: per sample we assigned negCD8_negIBA1 label to the ROI with the lowest sum of T cell and macrophages fraction, negCD8_posIBA1 to one of remaining ROI with lowest fraction of T cells, posCD8_negIBA1 to one of remaining ROI with lowest fraction of macrophages, and posCD8_posIBA1 to the remaining ones (Figure S5G). Using this procedure, we relabeled 43 out of 168 ROIs.

### GeoMx pathway activity analysis and correlation analysis on the deconvoluted transcriptomic signal

We used deconvoluted macrophage and T cell specific transcriptomics profiles to further explore the activity of key pathways connected to the biology and immune response of these cells. We selected 24 macrophage-related and 44 T cell-related pathways from MSigDB database,[104] from Canonical Pathways and Gene Ontology: Biological Processes collections, to compare their activities within different types of AOI and clinical features of the patients. T cell exhaustion related gene set was retrieved from Andreatta et al. and Zheng et al.[48] Macrophage M1/M2 signatures and myeloid T cell attraction/repression signatures were derived from Wang et al.[107] and Tietscher et al.[108] Additional pathways were derived from our scRNA-seq dataset as differentially expressed genes with >0.5Log2FC between: CD163 vs ITGAX macrophages (M1/M2 signature), $NECTIN^+$ vs $NECTIN^-$ macrophages, TIGIT/$CD226/CD96^+$ vs TIGIT/$CD226/CD96^-$ $CD8^+$ T cells). The full list of selected pathways can be found in Tables S3 and S4. Q3 normalized gene expression matrix was used for pathway analysis. Selected pathway activities were inferred using the GSVA method with Poisson kernel from the GSVA[105] R package.

Statistical significance of the differences between pathways activities between IDS and chemo-naive samples, per each AOI type, was assessed using a two-sided Wilcoxon rank-sum test.

Finally, we calculated Pearson correlation coefficient scores to analyze the connections between pathway GSVA scores and fraction of main TME cell types (tumor cells, macrophages and T cells) obtained from BayesPrism. We calculated correlation coefficients and p-values for all pathway combinations and displayed the results in a heatmap, showing only statistically significant correlations.

### WGS and SBS3

WGS was performed as previously described.[10] Samples with a tumor purity <10% were excluded. COSMIC single base substitution reference signatures v3.3.1[109] were used, adjusted for trinucleotide frequency as reported in.[75] HRD samples were defined as those with a positive SBS3 (Sig3) status and computed as described in.[75]

### Genomic homologous recombination deficiency scoring

OvaHRDscars were calculated using the package ovaHRDscar (https://github.com/farkkilab/ovaHRDscar) as described in our previous publication using either WGS or SNP-array data.[77] ovaHRDscar package quantifies three types of allelic imbalances: loss of heterozygosity, telomeric allelic imbalances and large scale transitions of certain characteristics. For WGS data, calculation was based on copy-number profiles estimated with PURPLE[110] using structural variants from GRIDSS2.[111] A cutoff value of ovaHRDscar >= 54 was used to define HRD positivity. Samples with a tumor purity <10% were excluded from calculations.

### Bulk RNA-seq data analysis

Fifty omental samples from 25 patients collected before NACT and at IDS were subjected to RNA sequencing. The preprocessing of bulk RNA sequencing reads was conducted using the SePIA pipeline[112] within the comprehensive Anduril framework[113] as previously described.[51] For the batch correction, the POIBM method was used with default parameters.[114] We employed the statistical framework PRISM[51] to decompose the gene-level effective read counts into cancer, immune, and stromal-specific signals. To assess the proportion of tumor, stromal, and immune cell subtypes, we employed the Kassandra deconvolution algorithm[115] using transcripts-per-million (TPM) expression values as input. To characterize the tumor proliferation rate, we acquired the expression of the genes related to the tumor proliferation rate functional signature, as was previously described.[116] To evaluate transcription factor activity, we used the DecoupleR framework v1.4.3[94] in Python and accessed the CollecTRI gene regulatory network[117] using decoupler.get_collectri(). We inferred TF enrichment scores using the univariate linear model approach with decoupler.run_ulm(), using gene- level statistics from DESeq2[118] output (stat value) as input. For comparing the expression of selected genes, we utilized the trimmed mean of M-values (TMM) of the genes.

### iPDCs generation and drug testing

The tissue for these experiments was obtained from five chemo-naive HGSC patients and six chemo-exposed HGSC patients from the ONCOSYS-Ova prospective cohort. iPDCs were generated from the harvested tissue following the protocol described by Nagaraj et al.[57] Briefly, freshly resected tumor pieces were finely minced and mildly digested with 1 U/mL Dispase II (Sigma- Aldrich, D4693) and 5 U/mL RQ1 RNase-free DNase I (Promega, M6101) in AdF+++ medium [DMEM/F-12 (Gibco) supplemented with 1X Glutamax (Gibco, 35050061), 10 mM HEPES (Sigma- Aldrich, H0887), and 1% v/v Pen/Strep (Gibco, 15140122)]. The resulting cell suspension was washed and resuspended in the RBC lysis buffer (Roche, 11814389001). Subsequently, cells were washed again, and cell count and viability were assessed using a LUNA™ *fl* Dual Fluorescence Cell Counter (Logos Biosystems). Then, cells were resuspended in complete medium (Advanced DMEM/F-12, Gibco) supplemented with cytokines and growth factors as reported elsewhere,[57] and seeded in ultra-low attachment 48-well suspension culture plates (Greiner Bio-One, 677102), embedded in an omentum gel-based matrix at a cell density of 1x10^3 cells/μL. The next day, iPDCs were treated with pembrolizumab (Selleck Chemicals, A2005) and tiragolumab (Selleck Chemicals, A2028) as single agents and in combination. The doses for pembrolizumab were selected based on previous work on effective doses in the same model system,[57] and tiragolumab concentrations were based on literature reports.[70] After 2-4 days, cells were harvested, and $CD8^+$ T cell activation was estimated by measuring the expression levels of granzyme B, IFN-γ, and Ki-67 using multiparameter flow cytometry. Samples were run on a BD LSRFortessaTM cell analyzer (BD Biosciences), and details about the employed antibodies are listed in STAR Methods and Table S7. Resulting flow cytometry data was analyzed using FlowJo™ v10.9.0 Software (BD Life Sciences), CYTO,[119] and TRIBUS,[34] and cell proportions and heatmaps were plotted using R scripts.

## QUANTIFICATION AND STATISTICAL ANALYSIS

Statistical analyses were performed using R version 4. The threshold for significance was set up as less or equal to 0.05 in all analyses. Statistical tests related to figures are indicated in the figure legends and further statistical details of the analyses are defined in the corresponding method sections. Number of individuals or samples in each test are explained in the results.